

1 Structure, transport and seasonality of the Atlantic Water Boundary

2 Current north of Svalbard: Results from a year-long mooring array

3 M. Dolores Pérez-Hernández^{1,2}, Robert S. Pickart¹, Daniel J. Torres¹,
4 Frank Bahr¹, Arild Sundfjord⁶, Randi Ingvaldsen⁴, Angelika H.H. Renner⁴, Agnieszka
5 Beszczynska-Möller³, Wilken-Jon von Appen⁵, Vladimir Pavlov⁶

6
7 1. Department of Physical Oceanography, Woods Hole Oceanographic Institution, Woods Hole, Massachusetts,
8 USA

9 2. Marine and Freshwater Research Institute, Reykjavik, Iceland

10 3. Institute of Oceanology Polish Academy of Sciences, Sopot, Poland

11 4. Institute of Marine Research, Tromsø, Norway

12 5. Alfred Wegener Institute, Helmholtz Centre for Polar and Marine Research, Bremerhaven, Germany

13 6. Norwegian Polar Institute, Tromsø, Norway.

14
15 **Keywords:** Atlantic Water, Svalbard Branch, A-TWAIN, seasonality, Arctic Ocean, Fram
16 Strait Branch

17 **Key Points:**

18 Main point #1: The 2012-13 average volume transport of the Atlantic Water
19 boundary current north of Svalbard is 2.08 ± 0.24 Sv.

20 Main point #2: The transport is maximum in late-summer to early-fall when
21 the Atlantic Water is warmest and saltiest.

22 Main point #3: The Atlantic Water layer is ventilated locally via convective
23 overturning in winter and early-spring before ice is advected into the region.

24 **ABSTRACT**

25
26
27
28 The characteristics and seasonality of the Svalbard branch of the Atlantic Water (AW)
29 boundary current in the Eurasian Basin are investigated using data from a six-mooring
30 array deployed near 30°E between September 2012 and September 2013. The instrument
31 coverage extended to 1200 m depth and approximately 50 km offshore of the shelfbreak,
32 which laterally bracketed the flow. Averaged over the year, the transport of the current
33 over this depth range was 3.96 ± 0.32 Sv (1 Sv= 10^6 m³ s⁻¹). The transport within the AW
34 layer was 2.08 ± 0.24 Sv. The current was typically sub-surface intensified, and its
35 dominant variability was associated with pulsing rather than meandering. From late-
36 summer to early-winter the AW was warmest and saltiest, and its eastward transport was
37 strongest (2.44 ± 0.12 Sv), while from mid-spring to mid-summer the AW was coldest and

38 freshest and its transport was weakest (1.10 ± 0.06 Sv). Deep mixed-layers developed
39 through the winter, extending to 400-500 m depth in early-spring until the pack ice
40 encroached the area from the north shutting off the air-sea buoyancy forcing. This vertical
41 mixing modified a significant portion of the AW layer, suggesting that, as the ice cover
42 continues to decrease in the southern Eurasian Basin, the AW will be more extensively
43 transformed via local ventilation.

44 **PLAIN LANGUAGE SUMMARY**

45 The Svalbard branch of the Atlantic Water (AW) flows eastward north of Svalbard
46 carrying warm and salty waters along the slope of the western Eurasian Basin. Here we
47 explore the characteristics and seasonality of the boundary current using data from a six-
48 mooring array deployed at 81.7°N, 30.6°E between September 2012 and September 2013.
49 On average the current carries 3.96 ± 0.32 Sv ($1 \text{ Sv} = 10^6 \text{ m}^3 \text{ s}^{-1}$), of which 2.08 ± 0.24 Sv
50 are of AW. From late-summer to early-winter the AW was warmest and saltiest, and its
51 eastward transport strongest, while from mid-spring to mid-summer the AW was coldest
52 and freshest and its transport weakest. In this region, the layer of AW is modified via
53 convective overturning in winter.

54

55 **1. INTRODUCTION**

56 One of the fundamental aspects of the Arctic Ocean is the circulation and
57 transformation of Atlantic Water (AW), which plays a critical role in Earth's climate
58 system. The modification and conversion AW within the Arctic domain form the
59 headwaters of the global meridional overturning circulation. It is well known that the AW
60 progresses through the Arctic as a system of cyclonic boundary currents (Rudels, 1994;
61 Aagaard and Carmack, 1994). However, to date there have been limited direct
62 measurements of the flow, and, as such, there are fundamental aspects of the current that
63 remain unknown. This includes robust quantification of its transport throughout the sub-
64 basins of the Arctic, the seasonality of the flow, and the detailed kinematic structure of the
65 boundary current system.

66 One of the two gateways through which AW enters the Arctic Ocean is Fram Strait,
67 between Greenland and Svalbard. The warm subtropical-origin water flows into the strait
68 via the West Spitzbergen Current (WSC). Averaged over the year, the WSC has an average
69 AW temperature of $3.1 \pm 0.1^\circ\text{C}$ and transport of 3.0 ± 0.2 Sv spanning the depth range 0-
70 250m (Beszczynska-Möller et al. 2012). The flow subsequently bifurcates into what is
71 known as the core WSC (1.3 ± 0.1 Sv) and the offshore WSC (1.7 ± 0.1 Sv) (Beszczynska-
72 Möller et al. 2012). The core WSC is baroclinically unstable with marked seasonality in
73 temperature, salinity, and stratification (Von Appen et al. 2016). It is difficult to detect a
74 seasonal signal in the velocity due to lateral shifts in the location of the current. The
75 offshore WSC, on the other hand, is weaker in summer than in fall/winter Beszczynska-
76 Möller et al. (2012).

77 Some portion of the offshore WSC recirculates within the strait and flows back to the
78 south as a boundary current over the Greenland slope (Hattermann et al. 2004; Håvik et al.
79 2017). Ultimately, three branches of AW emerge from the strait and enter the Arctic basin

80 (Figure 1): a branch encircling the Yermak Plateau (the Yermak Plateau Branch; e.g. Meyer
81 et al., (2017a)), a branch flowing through Yermak Pass (the Yermak Pass branch; Koenig et
82 al. 2017b), and a branch following the Svalbard continental slope (the Svalbard branch:
83 Cokelet et al. 2008; Våge et al. 2016; Hernández et al. 2017; Kolås and Fer 2018). Recent
84 model simulations, supported by observations in the Yermak Pass, indicate that the
85 transport is divided predominantly between the Svalbard Branch (annual mean 0.4 Sv) and
86 Yermak Pass Branch (0.9 Sv), with only a minor fraction comprising the Yermak Plateau
87 Branch (0.04 Sv) (Koenig et al. 2017a). These numbers imply that all of the offshore WSC
88 recirculates in Fram Strait; however, it must be kept in mind that there is considerable
89 uncertainty in both the measurements and model values.

90 North of Svalbard, the AW in the Svalbard branch interacts with sea-ice, and the
91 resulting melt water isolates it from the sea surface (Polyakov et al. 2011; Ivanov et al. 2009;
92 Rudels 2013; Onarheim et al. 2014; Rudels et al. 2014; Renner et al. 2018). Using data from
93 a single mooring deployed for two years north of Svalbard, Ivanov et al. (2009) provided
94 the first seasonal description of the AW downstream of Fram Strait, determining that the
95 temperature maximum occurs later in the fall than in Fram Strait. This was further
96 documented using more recent data from a mooring located in the same region (Randelhoff
97 et al. 2015). These authors addressed the seasonality of nitrogen and chlorophyll as well,
98 finding that nitrogen concentrations were minimum in summer when primary production
99 peaked due to the onset of ice melt and enhanced stratification. Using data from the same
100 mooring, Renner et al. (2018) determined that, even though advection accounts for 80% of
101 the seasonal heat budget, there is a sizable contribution from local processes such as tidal
102 mixing and air-sea exchange.

103 Shipboard surveys north of Svalbard have shed light on other aspects of the AW
104 boundary current there (Våge et al. 2016; Pérez-Hernández et al. 2017). The current is 30-40

105 km wide and covers the approximate depth range of 75-700 m, with a varying kinematic
106 structure. The flow can at times be surface intensified, while other times it is bottom
107 intensified. The current is baroclinically unstable and can meander across the slope. Both
108 anti-cyclones and cyclones appear to be spawned by the current in this region, the former
109 containing AW in their core. This is consistent with the modeling study of Crews et al.
110 (2018). The mean volume transport of AW computed from a series of shipboard transects
111 occupied in September 2013 was 2.3 ± 0.3 Sv. This agrees with the upstream summer/fall
112 transport estimates of the WSC presented by Koenig et al. (2017b) and Beszczynska-Möller
113 et al. (2012) (2.4 Sv and 2.5 Sv, respectively). This implies that the three AW branches
114 emerging from Fram Strait eventually merge with the Svalbard branch north of Svalbard and
115 that there is no recirculation in Fram Strait during summer/fall. Koenig et al. (2017b) argue
116 that Yermak Pass branch merges quickly with the Svalbard branch to the east of the pass.

117 Farther to the east (ca. 60°E and eastward), the eastward flow of AW is called the “Fram
118 Strait branch”. In the vicinity of Franz Joseph Land, Pnyushkov et al. (2015) found that the
119 maximum AW temperatures occurred in March, while north of the Laptev Sea, Dmitrenko
120 et al. (2006) and Pnyushkov et al. (2015) observed higher/lower temperature and salinity
121 in winter/summer for AW. On the other hand, Pnyushkov et al. (2018) showed higher AW
122 transports in June (ca. 9.9 Sv) than in April (ca. 0.3 Sv). Dmitrenko et al. (2006) attributed
123 some of the seasonality in the Laptev Sea to lateral shifts of the AW. In particular, the
124 current moved towards the slope in winter and away from the slope in summer. Several
125 studies have documented how the AW advected in the Fram Strait branch mixes with the
126 AW outflow from the Barents Sea via the St. Anna Trough. Above 600 m depth, the
127 mixture is believed to be roughly equal, while deeper than this the AW signature stems
128 mainly from the Barents Sea outflow (Schauer et al. 1997; Pnyushkov et al. 2018). This

129 mixing process makes it more difficult to relate the seasonality of the current east of 70 °E
130 to that farther upstream (Schauer et al. 1997; 2002; Dmitrenko et al. 2015).

131 Part of the challenge in quantifying the structure and seasonal behavior of the Svalbard
132 branch of the AW is that the mooring measurements to date have been sparse, while
133 shipboard surveys generally occur during the ice-free months of the year. In 2012 the
134 “Long-term variability and trends in the Atlantic Water inflow region” (A-TWAIN)
135 program was initiated to enhance our understanding of the flow of AW north of Svalbard.
136 As part of the program, a high-resolution mooring array was deployed across the current
137 to the base of the continental slope for one year near 30°E. This represented the first time
138 that the AW boundary current in the western Eurasian basin was measured with such an
139 extensive array (Figure 1). The goal was to quantify the transport of the current over the
140 full seasonal cycle, determine its kinematic and water mass structure, and address the role
141 of external forcing (e.g. air-sea buoyancy fluxes, wind, ice) in dictating the variability. The
142 two shoreward-most moorings have already been used to investigate the hydrography and
143 nutrients (Randelhoff et al. 2015) and to quantify the processes controlling the local heat
144 budget in the upper part of the water column (Renner et al. 2018).

145 Here we present the first results from the full A-TWAIN mooring array deployed
146 northeast of Svalbard from autumn 2012 to autumn 2013. The paper is organized as
147 follows. Section 2 presents the dataset and methodology used for the study. Section 3.1
148 describes the year-long average structure of the current, and Section 3.2 presents the
149 dominant variability in this structure. The seasonal cycle is investigated in Section 3.3,
150 which is then related to the seasonality at two upstream locations in Section 3.4 to assess
151 the role of advection. In Section 3.5 the properties and evolution of the mixed-layer are
152 examined and related to driving mechanisms. Section 3.6 addresses how the AW layer is
153 modified through the year. The work is summarized in section 4.

154

155 **1. DATA AND METHODS**

156 **1.1. MOORING MEASUREMENTS**

157 From September 24, 2012 to September 15, 2013 a mooring array was maintained
158 across the Svalbard branch of the AW boundary current, centered at 81.7°N and 30.5°E, as
159 part of the international A-TWAIN project (Figure 1). Eight moorings were deployed,
160 extending from the outer shelf to the deep continental slope. Unfortunately, the mooring
161 situated near the 500 m isobath was lost (presumably due to fishing activity), and the
162 outermost mooring did not return any usable data. Nonetheless, the six remaining moorings
163 provided the first extensive coverage of the boundary current north of Svalbard. The
164 distances between the moorings ranged from approximately 10 km to 15 km, which is
165 larger than the local Rossby radius of deformation which is order 8 km (Nurser and Bacon
166 2014; Zhao et al. 2014).

167 The two inshore moorings were provided by the Norwegian Polar Institute (NPI) and
168 the Institute of Marine Research (IMR), while the four offshore most moorings were
169 provided by the Woods Hole Oceanographic Institution (WHOI). The inshore moorings
170 contained Sea-Bird MicroCat and SeaCat conductivity-temperature-depth sensors (CTDs)
171 and two kinds of current measurements: acoustic Doppler current profilers (ADCPs) with
172 a vertical resolution of 4 m (standar deviation 1.86 cm/s), and Aanderaa RCM7 point
173 current meters (standar deviation 0.16 cm/s). See Table 1 and Sundfjord et al. (2017) for
174 details. The WHOI moorings consisted of McLane Moored Profilers (MMPs) that sampled
175 the water column between 100-1250 m depth every 12 hours. Both Sea-Bird and Falmouth
176 Scientific Instrument CTD sensors were used. The vertical profiles had a resolution of 2
177 m. MicroCats were situated on the top floats and beneath the bottom stops of the profilers,
178 to aid in the calibration of the MMPs. Velocity was measured on the WHOI moorings with

179 an upward-facing 300 kHz workhorse ADCP (standard deviation 0.50 cm/s) and a
180 downward-facing 75 KHz Long Ranger ADCP (standard deviation 1.67 cm/s), with a
181 vertical resolution of 4 m and 15 m, respectively (see Table 1). The range of the downward-
182 facing ADCPs was approximately 400 m. The velocity records were low-passed using a
183 2nd order 36-hr Butterworth filter to remove the tidal and inertial signals. The accuracy of
184 each instrument is given in Table 2.

185 The moored CTD sensors underwent pre- and post-deployment laboratory calibrations,
186 and were further evaluated using shipboard CTD casts (obtained with a Sea-Bird 911+
187 whose conductivity was calibrated using water samples) from the deployment and recovery
188 cruises (Våge et al. 2016; Pérez-Hernández et al. 2017). The MMP profiles were processed
189 using a set of WHOI-based software routines (available at flotsam.whoi.edu) which
190 involves removing spikes, analyzing sensor lags, and removing density inversions. In
191 addition, the MMPs were calibrated by comparison to Sea-Bird MicroCats located just
192 below the MMP bottom stop. The conductivity sensor on the WHOI3 MMP failed at the
193 start of the deployment period. We created a synthesized salinity record at this site based
194 on the temperature/salinity relationship at the two bounding moorings.

195 Vertical sections of potential temperature (θ), salinity (S), and potential density (σ_θ)
196 were created using Laplacian-spline interpolation with a grid spacing of 10 km in cross-
197 stream distance (x) and 60 m in depth (z) for every time step. Because the ADCP
198 measurements on the continental slope only reached ~500 m depth, we constructed vertical
199 sections of absolute geostrophic velocity in order to extend the coverage to the full depth
200 range of the MMPs. These sections were computed following the methodology of
201 Fratantoni et al. (2001). For each individual section, the boundary current was defined for
202 that time step as the area where the velocity was > 10% of the maximum velocity in the
203 section. This definition was altered when features such as eddies were clearly present

204 offshore of the boundary current. The AW portion of the boundary current was determined
205 in the same manner as was done in Pérez-Hernández et al. (2017). In particular, AW is
206 defined as $\theta \geq 1^\circ\text{C}$, $S \geq 34.9$, and $\sigma_\theta \geq 27.6 \text{ kg m}^{-3}$. Transport errors are expressed as
207 standard deviations.

208 We also make use of data from a single mooring maintained by the Institute of
209 Oceanology, Polish Academy of Sciences (IOPAN) that was positioned north of Svalbard
210 approximately 140 km to the west of the A-TWAIN array during the same year (see Figure
211 1a for the location of the IOPAN mooring). The mooring was situated at the 800 m isobath
212 and contained an MMP that profiled the water column between 50 and 750 m every 12 hrs.
213 The CTD data were calibrated and processed in similar fashion to the A-TWAIN data (see
214 Renner et al. 2018).

215 We also compare our results with Fram Strait using data from a MicroCat situated on
216 the F3-15 mooring located at 78.831°N , 8.005°E in a water depth of 1010 m. The MicroCat
217 nominally resided at 57m depth. However, due to severe mooring blowdowns, the
218 instrument on average was at 117m depth (von Appen et al. 2015). Hence, the MicroCat
219 measures the warmer (shallower) part of the AW layer in the WSC.

220 **1.2. REANALYSIS DATA**

221 To document the regional wind field during the study period we use the ERA-Interim
222 daily global atmospheric reanalysis product. The data were downloaded from the European
223 Centre for Medium Range Weather Forecast public datasets
224 (<http://apps.ecmwf.int/datasets/>). The spatial resolution is 0.75 degrees and the temporal
225 resolution is 12 hours (Dee et al. 2011).

226 **1.3. SEA ICE CONCENTRATION DATA**

227 The MASAM2 sea ice concentration (Fetterer et al. 2015) was downloaded from the
228 National Snow and Ice Data Center (<https://nsidc.org/data/docs/noaa/g10005-masam2/>).

229 This sea ice product has a 4 km resolution and blends sea ice extent from the Multisensor
230 Analyzed Sea Ice Extent (MASIE) product and sea ice concentration from the Advanced
231 Microwave Scanning Radiometer 2 (AMSR2). This product is more accurate than using
232 AMSR2 alone as it uses microwave and infrared measurements (see
233 <http://nsidc.org/data/G10005>).

234 **1.4. MIXED-LAYER ANALYSIS**

235 Properties of the mixed-layer were analyzed using the MMP data from the WHOI and
236 IOPOAN moorings, which had top floats at depths of 100 m and 50 m, respectively.
237 Therefore, we could only document the periods when the mixed-layers exceeded these
238 depths. At each time step, the depth of the mixed-layer was determined following the
239 method of Pickart et al. (2002a). This involves making an initial estimate visually, then
240 computing a two-standard deviation envelope over this portion of the profile. The mixed-
241 layer depth is then determined objectively as the depth where the profile passes out of this
242 envelope. A linear fit is then made to the mixed-layer profile for θ , S , and σ_θ , the average
243 of which is taken to be the value of the mixed-layer for the variable in question. For
244 mooring WHOI3, where the salinity (and hence density) profiles were determined
245 synthetically, we used the temperature profiles to determine the mixed-layer depths.

246 One-dimensional mixed-layer modeling was carried out using the model of Price et al.
247 (1986). The model is forced using the ERA-Interim data and initialized with the 0600
248 November 3, 2012 profiles of θ , S , and σ_θ from the WHOI1 mooring. This is the first time
249 that the mixed-layer at the site extended deeper than 100 m (the upper measurement limit
250 of the MMP). The hydrographic profiles were extrapolated to the sea surface. As time
251 progresses, if the density profile becomes unstable, the model mixes the water column until
252 it attains static stability (increasing density gradient), mixing layer stability (bulk
253 Richardson number), and shear flow stability (gradient Richardson number). Sensitivity

254 tests were run where the model was forced either with wind-stress, heat flux, freshwater
255 flux, or different combinations of these. The effects of the wind and freshwater forcing
256 were found to be negligible, hence the model was forced with heat flux only.

257

258 **2. RESULTS**

259 **2.1. YEAR-LONG AVERAGE**

260 The year-long mean flow vectors (from the ADCPs), averaged over the full water
261 column, show that the boundary current is strongest on the upper continental slope (Figure
262 2a). Progressing offshore the current weakens and the vectors rotate to the northeast,
263 generally following the topography. (It is unclear why the WHOI-1 vector is directed
264 eastward and hence onshore; this could be due to small scale variations of the bathymetry
265 not captured in the IBCAO v3 data set.) The standard error ellipses are included on Figure
266 2, indicating that the mean flow is statistically significant everywhere (the average integral
267 time scale across the array was 5.7 days). It is clear that, in the mean, the array bracketed
268 the boundary current: the flow at the offshore-most mooring WHOI4 is weak, as is the flow
269 at the inshore-most mooring NP1, which is directed off the shelf.

270 Averaged over the year, the wind speed at the array site was 6.7 m/s from the southeast,
271 while the ice cover ranged from 45% on the shelf to 55% at the offshore mooring location
272 (Figure 3a). The mean vertical sections for the year-long deployment are shown in Figures
273 3b-d, where we have indicated the location of the AW layer (bounded by the dashed lines
274 in the figure). As noted above we adopted the same definition for AW that was used in
275 Pérez-Hernández et al. (2017); namely, AW corresponds to $\theta \geq 1^\circ\text{C}$, $S \geq 34.9$, and $\sigma_\theta \geq$
276 27.6 kg m^{-3} . One sees that the AW layer roughly spans the depth range 150–600 m, and
277 that the temperature maximum is shallower and displaced farther offshore than the salinity
278 maximum. Above the AW layer, Polar Surface warm Water (PSWw) can be found at times

279 with lower salinities than AW. Below the AW layer is Arctic Intermediate Water (AIW)
280 (see also Pérez-Hernández et al., 2017).

281 The vertical section of averaged absolute geostrophic velocity shows eastward flow
282 across the entire array, with a core value of ~ 17 cm/s near the continental slope (Figure
283 3d). The maximum flow likely would have been measured at the 500m isobath mooring,
284 which was lost. Based on various testing, we chose the grid spacing and interpolation
285 parameters in a way to limit any unrealistic extrapolation in this region of missing data.
286 The mean core velocity is similar to other reported synoptic estimates in the literature (e.g.
287 Schauer et al. 2002; 2004; Pnyushkov et al. 2015; Meyer et al. 2017a). Based on our criterion
288 of 10% of the core absolute geostrophic velocity to define the outer edge of the current,
289 the array bracketed the entire current in the mean (i.e. the 10% contour is inshore of
290 mooring WHOI4). The mean current is subsurface intensified, corresponding to the
291 upward-sloping isopycnals towards the coast in the upper layer, and a slight downward tilt
292 of the deep isopycnals (recall that the section displays absolute geostrophic velocity). It
293 should be noted that previous shipboard realizations of the current implied that it was just
294 as apt to be surface intensified (Våge et al., 2016; Pérez-Hernández et al., (2017), which is
295 not supported by the year-long mooring data. Offshore of the core, the flow is mainly
296 barotropic. The e-folding width of the current is 67.5 km.

297 Based on the mean section, the transport of the boundary current at this location is 3.96
298 ± 0.32 Sv to the east, of which 2.08 ± 0.24 Sv is AW, 0.99 ± 0.18 Sv AIW, and 0.26 ± 0.12
299 Sv PSWw (Table 3). This value of AW transport is in line with the reported synoptic
300 estimates from the deployment and recovery cruises of the array, 1.8 ± 0.3 Sv and $2.31 \pm$
301 0.29 Sv, (Våge et al. 2016; Pérez-Hernández et al. 2017 respectively). While there is also
302 agreement in the transport of PSWw between the mooring array and the shipboard surveys,

303 the same is not true for the AIW simply because the depth range of the mooring data
304 exceeds that of the shipboard measurements.

305 The AW volume transport reported here is the first year-long mean estimate based on
306 a mooring array in the western Nansen Basin that resolves and brackets the current. It is
307 therefore of interest to compare our value with the mooring-based year-long mean estimate
308 in Fram Strait. As noted in the introduction, Beszczynska-Möller et al. (2012) computed an
309 average AW (defined as $>2^{\circ}\text{C}$) northward transport in Fram Strait of 3.0 ± 0.2 Sv ($1.3 \pm$
310 0.1 Sv in the core WSC and 1.7 ± 0.1 Sv in the offshore WSC), compared to our year-long
311 mean value of 2.08 ± 0.24 Sv near 30°E . This difference suggests two possibilities: (1)
312 Roughly 1 Sv of the offshore WSC recirculates in Fram Strait and all of the remaining
313 transport ends up in the Svalbard branch by the longitude of the A-TWAIN site, which
314 implies that the Yermak Plateau and Yermak Pass branches merge quickly with the
315 Svalbard branch. This is consistent with the results of Koenig et al., 2017b); (2) Less of
316 the offshore WSC recirculates in Fram Strait, which implies that not all of the Yermak
317 Plateau and Yermak Pass branches have joined the Svalbard branch by the location of our
318 array. Regardless of which scenario applies, we stress that it is very difficult to identify
319 the AW in a consistent fashion between the A-TWAIN site and Fram Strait due to the
320 transformation of the water via ocean-ice-atmosphere interaction and mixing as it advects
321 eastward (Onarheim et al. 2014; Rudels et al. 2014; Pérez-Hernández et al. 2017; Meyer et al.
322 2017b). Also, Crews et al. (2018) estimate that around 10% of the AW is lost from the
323 boundary current north of Svalbard to anticyclonic eddies. Hence, even though both
324 Beszczynska-Möller et al. (2012) and our study define AW in an objective manner, it is hard
325 to make a precise comparison.

326

327 **2.2. STRUCTURAL VARIABILITY**

328 To assess the variability of the current, an empirical orthogonal function (EOF) analysis
329 was carried out using the absolute geostrophic velocity sections. A dominant mode
330 emerged, accounting for nearly 70% of the overall variance, which corresponds to a pulsing
331 of the boundary current. This is visualized by adding the maximum/minimum values of the
332 mode into the mean section (Figures 4a and b). In the maximum state, the core of the
333 current is nearly three times stronger than the minimum state. In both states, the current is
334 bottom intensified. When the boundary current is stronger, a counter flow (to the west)
335 develops over the outer shelf. The principle component time series for mode 1 shows that
336 the current was strongest from mid-July to mid-August (Figure 4c).

337 The shipboard sections presented in Pérez-Hernández et al. (2017), occupied over a
338 two-week period while the mooring array was being recovered in September 2013, showed
339 the boundary current in a surface-intensified state. Furthermore, the sections revealed that
340 the current can meander across the slope. While the mooring data indicate that this scenario
341 does occur at times, it is much more common for the boundary current to be bottom-
342 intensified and to vary in strength, rather than in cross-slope position.

343

344 **2.3. SEASONALITY**

345 During the year-long deployment of the array, the wind was quite variable with no
346 preferred direction (Figure 5a). This is due to the large number of storms that propagate
347 through this region (Bengtsson et al. 2006). The strongest wind speeds occurred between
348 mid-December 2012 and mid-January 2013, reaching up to 20 m/s (Figure 5b). Over the
349 course of the year there were three general ice regimes: nearly open water (average
350 concentration of 5%) from early-September to mid-December (this period included two
351 calendar years); partial ice concentration from mid-December to early-April and again from

352 early-August to early-September; and consolidated ice cover from early-April to early-
353 August (i.e. in between the two partial ice periods, Figure 5c).

354 The properties and strength of the boundary current varied in accordance with these ice
355 regimes. The mean depth-averaged vectors for the open water and full-ice cover periods
356 are shown in Figures 2b and c, respectively. This reveals that the core of the boundary
357 current was stronger when there was no ice. The time series in Figure 5d also show that
358 the current was warmest, saltiest, and had the largest volume transport during the open
359 water period, while during the time of partial ice cover following the open water period it
360 cooled, freshened, and decreased in transport. When the region was nearly fully ice covered
361 the current remained relatively cold, fresh, and weak. Note that, starting in early-February
362 after the sharp transition in boundary current properties, the current continued to cool
363 slightly until the early summer, but became systematically saltier over this period. Not
364 until the partial ice period in August did the pronounced warming and salinification
365 commence.

366 To further explore this seasonality, we constructed composite average vertical sections
367 of different properties for the open water period versus the full ice cover period (Figure 6).
368 In the former, the AW is warmest and saltiest over the upper-slope, spanning a depth range
369 from nearly 600 m to the top of our data coverage at 100 m (Using data from the NPI
370 moorings only, which have instruments shallower than the WHOI moorings, Renner et al.
371 (2018) showed that the AW at times reached as shallow as 25 m). A region of enhanced
372 stratification extends over much of the layer. The total volume transport of the boundary
373 current is 3.30 ± 0.13 Sv, of which 2.44 ± 0.12 Sv is AW (Table 3). By contrast, when the
374 ice cover is heavily consolidated, the property core of the AW is located farther offshore
375 and the layer is considerably thinner over the upper-slope. The stratification is significantly
376 weaker as well. The total eastward transport of the boundary current is 2.32 ± 0.06 Sv of

377 which 1.10 ± 0.06 Sv is AW (Table 3). Hence, going from the open water period to the
378 time of nearly complete ice cover, the AW core on average becomes 0.84°C colder, 0.034
379 fresher, and its volume transport diminishes by 1.34 Sv.

380 The waters bounding the AW also exhibit changes between these two seasons. The
381 fresh upper layer of PSWw, barely present during the open water period, expands during
382 the full ice cover period to nearly 200 m depth. However, the velocity of the PSWw is
383 smaller during this time period so that, despite the increase in cross-sectional area, the
384 volume flux remains approximately the same at 0.30 ± 0.01 Sv (Table 3). Note that in the
385 vicinity of the shelfbreak the water becomes markedly colder and fresher, and the velocity
386 reverses. This suggests that, at this time of year, the flow on the shelf is westward
387 transporting a distinct water mass, perhaps melt water. Beneath the AW layer the properties
388 of the AIW also vary. In particular, the average temperature and salinity of the layer
389 changes by 0.06°C and -0.014 , respectively, during the later period (when the AW is
390 warmer and fresher). At the same time, the transport of the AIW layer approximately
391 doubles from 0.46 ± 0.07 Sv to 0.88 ± 0.05 Sv (Table 3). Overall, across the entire section
392 (i.e. to a depth of 1250 m), the AW accounts for 60% of the seasonal amplitude.

393

394 **2.4. CONTRIBUTION FROM UPSTREAM**

395 To get a deeper understanding of the seasonal cycle of AW, Figure 7 compares the
396 characteristics of the Svalbard Branch against that measured at two upstream locations –
397 in Fram Strait at the 117-meter depth MicroCat of mooring F3-15 (see von Appen et al.,
398 2016), and with the IOPAN mooring located 140 km to the west of the A-TWAIN array
399 (see Figure 1). Note that with the profiling instruments at the IOPAN and WHOI moorings
400 the average temperature of the AW layer can be calculated, while this is not possible for
401 the point measurement in Fram Strait.

402 Comparison of the temperature time series between the AW at the A-TWAIN site and
403 Fram Strait reveals a clear two-month lag, with Fram Strait leading (Figure 7, where we
404 have shifted the x-axis between the two sites accordingly). This is consistent with the
405 measured advective speeds of 16-18 cm/s at the Fram Strait location and the A-TWAIN
406 site. Such an advective velocity implies a lag of 40-70 days depending on whether a parcel
407 follows the slope route or the Yermak Pass route as suggested in Koenig et al. (2017). The
408 lag between the IOPAN mooring and the A-TWAIN site is approximately 5 days (see also
409 Renner et al., 2018). Curiously, while the AW temperatures at Fram Strait and north of
410 Svalbard display a very similar pattern (correlation of 0.7 and 0.8 for Fram Strait and
411 IOPAN, respectively, Figure 7a), salinity does not show such a clear relationship between
412 the Svalbard slope and Fram Strait (there is no significant correlation, Figure 7b). This
413 suggests that there may be local processes on the slope that affect the salinity more than
414 the temperature. We now explore the local modification of the water column at the A-
415 TWAIN and IOPAN sites via convective overturning driven by air-sea fluxes.

416

417 **2.5. MIXED-LAYER DEPTHS**

418 Mixed-layer depths (MLDs) were estimated following the methodology of Pickart et
419 al. (2002a) for the A-TWAIN array (for the moorings that employed CTD profilers) and
420 for the IOPAN profiling mooring. Figure 8a shows a representative mixed layer at each
421 site, and Figure 8b compares the time series of MLD between the IOPAN mooring and the
422 WHOI1 mooring (the shallowest of the WHOI moorings, which is closest in bottom depth
423 to the IOPAN site). We note that the top float of the IOPAN mooring was at 50 m depth
424 versus 100 m depth for the WHOI moorings. One sees that there is generally good
425 agreement between the two locations (separated by 140 km): the mixed-layers steadily
426 deepened from early-November until early-April when they abruptly became shallow (if a

427 mixed-layer wasn't observed at a given time step, then no symbol was plotted). The
428 transition to shallow MLDs corresponded to the onset of full ice cover in early-April
429 (Figure 5b). This implies that the ice was not locally formed, otherwise brine-driven
430 convection would have deepened the mixed-layer further (plus there was no evidence of
431 salinification of the mixed-layer at this time, see below). Randelhoff et al. (2015) observed
432 in the dataset of the NPI2 mooring that the stratification breaks down in December and the
433 MLD deepens, mixing near-surface cold and fresh water with the AW. Meyer et al. (2017a)
434 noted deeper MLDs in March versus June from drifting ice camps deployed north of
435 Svalbard. However, the deepest MLD recorded by Meyer et al. (2017a) was only 100 m.
436 To our knowledge, this is the first time that deep MLDs (exceeding 500 m) have been
437 observed on the continental slope of the Nansen Basin.

438 Are these measured MLDs consistent with the atmospheric forcing? To assess this, we
439 used the one-dimensional mixing model of Price et al. (1986) (hereafter referred to as the
440 PWP model). The model was initialized with the 06:00 UTC November 3, 2012 profile of
441 temperature, salinity, and density from the WHOI1 mooring, and forced with the ERA-
442 Interim reanalysis heat flux time series for the grid point closest to the mooring. The initial
443 hydrographic profile chosen was the first one of the year with a MLD that significantly
444 exceeded the depth of the mooring top float. We extrapolated the uppermost value to the
445 surface with the same value. When there was complete ice cover at the mooring site the
446 heat flux was set to zero. (We used a criterion of 85% ice concentration for this, but results
447 are not sensitive to the precise choice).

448 As seen in Figure 9, the model does a reasonable job reproducing the depth of the
449 observed mixed-layer. There is significantly more scatter in the data, but this is to be
450 expected based on the high degree of small-scale lateral variability that is present in regions
451 of active convection (Schott et al. 1996; Pickart et al. 2002b). Also, the model ignores lateral

452 advection and hence any upstream preconditioning (although we note that the WHOI1
453 mooring site is outside of the core of the boundary current where the mean speed is only
454 7-8 cm/s (Figure 6); also recall the good agreement in MLD between the WHOI1 mooring
455 and the IOPAN site (Figure 9)). From early-November until the time of 100% ice
456 concentration in early-April, the model MLD deepens in a manner that corresponds to a
457 low-pass of the observations. Once full ice cover sets in and the heat flux goes to zero, the
458 water column restratifies in accordance with the data (there are a small number of observed
459 MLDs exceeding 100m during this period). When the ice cover begins to decrease again
460 and transitions to open-water in late summer, the short-wave radiative heating dominates
461 the turbulent heat flux and so the model continues to show no mixed-layer, again consistent
462 with the observations. The importance of local air-sea fluxes is in line with the results of
463 Aagaard (1987) who, based on mooring measurements close to the A-TWAIN study area,
464 concluded that changes in water mass properties are due more to vertical heat fluxes than
465 lateral mixing. One-dimensional convection models forced by heat flux have also been
466 used previously to shed light on the mixed layer characteristics north of Svalbard (Ivanov
467 et al. 2016). In addition, Fer et al. (2017) used one-dimensional modeling to investigate the
468 evolution of the hydrographic properties in the upper water column in this region between
469 January and March. They found that vertical processes dominate as well, with a clear
470 dependence on the eddy diffusivity.

471 The impact of the deepening mixed-layer on the water column is seen clearly in the
472 anomaly plots of Figure 10, where we have differenced the vertical profiles of temperature
473 and salinity from their initial profiles, respectively (for each day we averaged the vertical
474 traces from all of the profiling moorings). Also shown on the plot are the depth of the
475 mixed-layers (green dots) as well as the upper and lower bounds of the AW layer (black
476 dots). This demonstrates how the AW layer becomes colder and fresher as it is ventilated

477 locally via convective overturning. Note that, before the full ice cover sets in (in early
478 April), the MLDs were occasionally approaching the depth of the lower boundary of the
479 AW layer. That is, nearly the entire layer was being transformed. Note also that, after local
480 convection ceased because of the ice cover, the part of the water column that was
481 previously ventilated remained anomalously cold and fresh until the end of the record. This
482 is likely due to the advection of transformed water from upstream.

483 Figure 10 (as well as Figure 9) demonstrate that the ventilation of the AW layer was
484 intermittent and there were times when the mixed-layer did not extend into the AW layer.
485 In these instances, the top interface of the AW reappeared (i.e. the upper black dots in
486 Figure 10). One can see that the water above the AW layer during these times was also
487 becoming colder, fresher and deeper as the season progressed, and some of these
488 occurrences were associated with a sudden drop in sea ice concentration (melting of
489 patches of sea ice advected over the array), for example in late-December and mid-March.

490 To elucidate the effect of the ice cover on the mixed-layers we separated the MLD time
491 series into three groups: full ice cover (concentrations greater than 85%), open water
492 (concentrations less than 10%), and partial ice cover (concentrations between 10% and
493 85%). These are shown in Figure 11 for both the IOPAN site and the A-TWAIN site. It is
494 clear that in highly consolidated ice the mixed-layers were generally shallow (when present
495 at all; the average MLD at the IOPAN and A-TWAIN sites are 71.2 m and 163.9 m,
496 respectively), due to the ice cover isolating the water column from the atmospheric forcing.
497 The few deep MLDs that appeared were likely ventilated within leads. Conversely, the
498 deepest mixed-layers formed when there was little to no ice cover (average MLD 275.9 m
499 and 249.8 m at the IOPAN and A-TWAIN sites, respectively). At the IOPAN site the MLD
500 exceeded 600 m in mid-March. During periods of partial ice cover the MLDs were highly
501 variable, ranging from very shallow to as deep as 400-500 m (average MLD 223.0 m and

502 259.4 m at the IOPAN and A-TWAIN sites, respectively). Our results are consistent with
503 Ivanov et al. (2016), who explored why the area north of Svalbard is ice-free in winter
504 (January-February). They found that summer ice decay allows a growing influence of
505 oceanic heat capacity (on a seasonal scale) and more favorable conditions for upwards heat
506 release through convective overturning.

507

508 **2.6. THE ATLANTIC WATER TRANSFORMATION**

509 It is instructive to consider the evolution of the mixed-layer throughout the year in T/S
510 space, which is displayed in Figure 12a. As mentioned earlier in the paper, PSWw resides
511 above the AW during part of the year. Additionally, an early stage of this water mass (in
512 late-summer) has also been discussed in the literature, the so called inshore Polar Surface
513 Water (iPSW) (Pérez-Hernández et al. 2017; Cokelet et al. 2008; Rudels et al. 2014). Using
514 shipboard data, Pérez-Hernández et al. (2017) found iPSW to be centered around 50 m.
515 For this reason, we use the data from the IOPOAN mooring whose profiles extend to 50 m
516 (the WHOI MMPs only sampled to 100m, and the NPI moorings did not have profilers).

517 One sees that the mixed-layer is ventilating iPSW in September, but, soon after, the
518 mixed-layer penetrates the AW. From November into December the mixed-layer remains
519 relatively warm but becomes saltier. However, in mid-December, sea ice starts to appear
520 on the surface which cools the surface layer (see Figure 10). This cold water subsequently
521 induces deeper mixed-layers until the end of March when the mixed-layer is at its densest.
522 Following the advent of near-complete ice cover at the end of March, the T/S character of
523 the mixed-layer changes abruptly since the layers are now quite shallow (Figures 8 and
524 10). At this point, for the remainder of the record, the mixed-layer ventilates the PSWw,
525 which becomes steadily warmer starting in April due to the lower contact with AW.

526 The T/S evolution of the part of the AW layer that is not locally ventilated at the IOPAN
527 site is shown in Figure 12b. There is a steady progression of this part of the layer to colder
528 temperatures and fresher salinities from the fall through the early-spring. These T/S
529 changes did not compensate each other in density, hence the lower part of the AW layer
530 became denser. Then, starting in May, this non-locally ventilated water became steadily
531 warmer and saltier through the end of August, although it remained somewhat denser. The
532 seasonal signal in salinity of this portion of the AW does not track the AW salinity in Fram
533 Strait, suggesting that lateral mixing takes place along the boundary current.

534

535 3. CONCLUSIONS

536 A six-mooring array was deployed between September 2012 and 2013 as part of the A-
537 TWAIN project to characterize the Svalbard Branch of the AW boundary current. The
538 dataset has offered the most extensive view to date of this current over a full year. The
539 vertical coverage of the moorings extended to 1200 m depth, and, averaged over the year,
540 the transport of the current over this depth range was 3.96 ± 0.32 Sv. The transport within
541 the AW layer was 2.08 ± 0.24 Sv, which agrees relatively well with previous quasi-
542 synoptic measurements from shipboard surveys (Våge et al. 2016; Pérez-Hernández et al.
543 2017). The current was, for the most part, sub-surface intensified, and its dominant
544 variability was associated with pulsing, rather than meandering.

545 Over the course of the measurement year there were three distinct seasonal periods.
546 From August to mid-December the AW temperature, salinity and transport were the
547 highest; during this time, the region was relatively ice free. From mid-December to April
548 the temperature and salinity decreased, reaching minimum values in February. Finally,
549 from April to the end of July, the temperature and transport were generally the lowest of
550 the year; during this period, the area was nearly fully ice-covered. The AW transport of

551 the Svalbard branch was 2.44 ± 0.12 Sv when the water was warmest and saltiest,
552 decreasing to 1.10 ± 0.06 Sv when the water was coldest and freshest.

553 The seasonal cycle of AW temperature at the A-TWAIN site was significantly
554 correlated with that in Fram Strait, with a two-month lag. This is consistent with the
555 estimated advective time between the two locations. A similar temperature seasonal cycle
556 has been described in the area using single moorings (Ivanov et al. 2009; Randelhoff et al.
557 2015; Renner et al. 2018). In the Barents Sea, maximum temperatures are found one month
558 earlier (September-October) than in our area (Lind and Ingvaldsen 2012). Farther to the east
559 the maximum/minimum AW temperature occurs in winter to spring/summer, which
560 suggests a further lag of several months with respect to the A-TWAIN region (Dmitrenko
561 et al. 2006; Pnyushkov et al. 2015).

562 Deep mixed-layers developed in the area from mid-October until April. At that point
563 sea ice encroached the region from the north and the concentration approached 100%. This
564 shielded the water column from the air-sea buoyancy flux, and consequently the mixed-
565 layers abruptly shallowed through meltwater input. The evolution of the mixed-layer depth
566 was well simulated using the one-dimensional PWP model forced with ERA-Interim
567 reanalysis heat flux time series from the region. From late-fall until early-spring the mixed-
568 layers became progressively deeper, ventilating the AW layer. The maximum mixed-layer
569 depth exceeded 500 m before the onset of full ice cover in April. This is the first time that
570 MLDs exceeding 150 m depth have been observed in the area. We suspect that the local
571 freshening of the AW layer is the reason for the disagreement between the Fram Strait AW
572 salinity signal and that recorded at the A-TWAIN site. These results suggest that as the ice
573 cover continues to decrease in the southern Eurasian Basin, the AW layer will be more
574 extensively modified via local ventilation. This will imply a lower heat and salinity flux
575 throughout the Arctic basin and enhanced dense water formation.

576

577 **4. ACKNOWLEDGMENTS**

578 We are grateful to the crew of the R/V *Lance* for the collection of the data. The U.S.
579 component of A-TWAIN was funded by the National Science Foundation under grant
580 ARC-1264098 as well as a grant from the Steven Grossman Family Foundation. The
581 Norwegian component of A-TWAIN was funded by the ‘Arctic Ocean’ flagship program
582 at the Fram Centre. The data used in this study are available at <http://atwain.who.edu> and
583 data.npolar.no (Sundfjord et al. 2017). The data from Fram Strait are available at
584 <https://doi.pangaea.de/10.1594/PANGAEA.853902>

585

586

587 **5. REFERENCES**

588

589 Aagaard, K., A. Foldvik, and S. R. Hillman, 1987: The West Spitsbergen Current: disposition
590 and water mass transformation. **92**, 3778–3784.

591 Appen, von, W. J., A. Beszczynska-Möller, and E. Fahrbach, 2015: Physical oceanography
592 and current meter data from mooring F3-15. *Pangea*,
593 doi:<https://doi.org/10.1594/PANGAEA.853902>.

594 Appen, von, W. J., U. Schauer, T. Hattermann, and A. Beszczynska-Möller, 2016: Seasonal
595 cycle of mesoscale instability of the West Spitsbergen Current. *Journal of Physical*
596 *Oceanography*, **46**, 1231–1254, doi:10.1175/JPO-D-15-0184.1.

597 Bengtsson, L., K. I. Hodges, and E. Roeckner, 2006: Storm Tracks and Climate Change.
598 <http://dx.doi.org/10.1175/JCLI3815.1>, **19**, 3518–3543, doi:10.1175/JCLI3815.1.

599 Beszczynska-Möller, A., E. Fahrbach, U. Schauer, and E. Hansen, 2012: Variability in
600 Atlantic water temperature and transport at the entrance to the Arctic Ocean, 1997-2010.
601 *ICES Journal of Marine Science: Journal du Conseil*, fss056.

602 Cokelet, E. D., N. Tervalon, and J. G. Bellingham, 2008: Hydrography of the West
603 Spitsbergen Current, Svalbard Branch: Autumn 2001. *Journal of Geophysical Research:*
604 *Oceans (1978--2012)*, **113**.

605 Crews, L., A. Sundfjord, J. Albrechtsen, and T. Hattermann, 2018: Mesoscale Eddy Activity
606 and Transport in the Atlantic Water Inflow Region North of Svalbard. *Journal of*
607 *Geophysical Research: Oceans*, **123**, 201–215, doi:10.1002/2017JC013198.

608 Dee, D. P., and Coauthors, 2011: The ERA-Interim reanalysis: Configuration and
609 performance of the data assimilation system. *Quarterly Journal of the Royal*
610 *Meteorological Society*, **137**, 553–597.

611 Dmitrenko, I. A., and Coauthors, 2015: Atlantic water flow into the Arctic Ocean through the
612 St. Anna Trough in the northern Kara Sea. *Journal of Geophysical Research: Oceans*,
613 **120**, 5158–5178.

614 Dmitrenko, I. A., I. V. Polyakov, and S. A. Kirillov, 2006: Seasonal variability of Atlantic
615 water on the continental slope of the Laptev Sea during 2002–2004. *Earth and Planetary*
616 *...*, **244**, 735–743, doi:10.1016/j.epsl.2006.01.067.

617 Fer, I., A. K. Peterson, A. Randelhoff, and A. Meyer, 2017: One-dimensional evolution of the
618 upper water column in the Atlantic sector of the Arctic Ocean in winter. *Journal of*
619 *Geophysical Research: Oceans*, **122**, 1665–1682,
620 doi:10.1002/2016JC012431@10.1002/(ISSN)2169-9291.NICE1.

621 Fetterer, F., J. S. Stewart, and W. N. Meier, 2015: *MASAM2: Daily 4-km Arctic Sea Ice*
622 *Concentration, 2012-2014*. Snow and Ice Data Center.

623 Fratantoni, P. S., R. S. Pickart, D. J. Torres, and A. Scotti, 2001: Mean structure and
624 dynamics of the shelfbreak jet in the Middle Atlantic Bight during fall and winter.
625 *Journal of Physical Oceanography*, **31**, 2135–2156, doi:10.1175/1520-

- 626 0485(2001)031<2135:MSADOT>2.0.CO;2.
- 627 Hattermann, T., P. E. Isachsen, W. von Appen, J. Albretsen, and A. Sundfjord, 2004: Eddy-
628 driven recirculation of Atlantic Water in Fram Strait. *Geophysical Research Letters*, **85**,
629 1259–1266, doi:10.1002/2016GL06832.
- 630 Håvik, L., R. S. Pickart, K. Våge, D. Torres, A. M. Thurnherr, A. Beszczynska-Möller, W.
631 Walczowski, and W. J. von Appen, 2017: Evolution of the East Greenland Current from
632 Fram Strait to Denmark Strait: Synoptic measurements from summer 2012. *Journal of*
633 *Geophysical Research: Oceans*, **122**, 1974–1994, doi:10.1002/2016JC012228.
- 634 Hernández, M. D. P., and Coauthors, 2017: The Atlantic Water boundary current north of
635 Svalbard in late summer. *Journal of Geophysical Research: Oceans*, **122**, 2269–2290,
636 doi:10.1002/2016JC012486.
- 637 Ivanov, V. V., and Coauthors, 2009: Seasonal variability in Atlantic Water off Spitsbergen.
638 *Deep Sea Research Part I: Oceanographic Research Papers*, **56**, 1–14,
639 doi:10.1016/j.dsr.2008.07.013.
- 640 Ivanov, V., V. Alexeev, N. V. Koldunov, I. Repina, A. B. Sandø, L. H. Smedsrud, and A.
641 Smirnov, 2016: Arctic Ocean Heat Impact on Regional Ice Decay: A Suggested Positive
642 Feedback. *Journal of Physical Oceanography*, **46**, 1437–1456, doi:10.1175/JPO-D-15-
643 0144.1.
- 644 Koenig, Z., C. Provost, N. Sennéchaël, G. Garric, and J.-C. Gascard, 2017a: The Yermak Pass
645 Branch: A Major Pathway for the Atlantic Water North of Svalbard? *Journal of*
646 *Geophysical Research: Oceans*, **122**, 9332–9349, doi:10.1002/2017JC013271.
- 647 Koenig, Z., C. Provost, N. Villaciers Robineau, N. Sennéchaël, A. Meyer, J. M. Lellouche,
648 and G. Garric, 2017b: Atlantic waters inflow north of Svalbard: Insights from IAOOS
649 observations and Mercator Ocean global operational system during N-ICE2015. *Journal*
650 *of Geophysical Research: Oceans*, **122**, 1254–1273, doi:10.1002/2016JC012424.
- 651 Kolås, E., and I. Fer, Hydrography, transport and mixing of the West Spitsbergen Current: the
652 Svalbard Branch in summer 2015. *ocean-sci-discuss.net*, doi:https://doi.org/10.5194/os-
653 2018-86.
- 654 Lind, S., and R. B. Ingvaldsen, 2012: Variability and impacts of Atlantic Water entering the
655 Barents Sea from the north. *Deep Sea Research Part I: Oceanographic Research Papers*,
656 **62**, 70–88, doi:10.1016/j.dsr.2011.12.007.
- 657 Meyer, A., and Coauthors, 2017a: Winter to summer oceanographic observations in the
658 Arctic Ocean north of Svalbard. *Journal of Geophysical Research: Oceans*, **122**, 6218–
659 6237, doi:10.1002/2016JC012391.
- 660 Meyer, A., I. Fer, A. Sundfjord, and A. K. Peterson, 2017b: Mixing rates and vertical heat
661 fluxes north of Svalbard from Arctic winter to spring. *Journal of Geophysical Research-*
662 *oceans*, **122**, 4569–4586, doi:10.1002/2016JC012441.
- 663 Nurser, A. J. G., and S. Bacon, 2014: The Rossby radius in the Arctic Ocean. *Ocean Sci*, **10**,
664 967–975, doi:10.5194/os-10-967-2014.

- 665 Onarheim, I. H., L. H. Smedsrud, R. B. Ingvaldsen, and F. Nilsen, 2014: Loss of sea ice
666 during winter north of Svalbard. *Tellus A*, **66**.
- 667 Pérez-Hernández, M. D., and Coauthors, 2017: The Atlantic Water boundary current north of
668 Svalbard in late summer. *Journal of Geophysical Research: Oceans*, **122**, 2269–2290,
669 doi:10.1002/2016JC012486.
- 670 Pickart, R. S., D. J. Torres, and R. A. Clarke, 2002a: Hydrography of the Labrador Sea during
671 active convection. *Journal of Physical Oceanography*, **32**, 428–457.
- 672 Pickart, R. S., D. J. Torres, and R. A. Clarke, 2002b: Hydrography of the Labrador Sea during
673 Active Convection. *Journal of Physical Oceanography*, **32**, 428–457, doi:10.1175/1520-
674 0485(2002)032<0428:HOTLSD>2.0.CO;2.
- 675 Pnyushkov, A. V., I. Polyakov, R. rember, M. B. Alkire, I. M. Ashik, T. M. Bauman, G. V.
676 Alekseev, and A. Sundfjord, Heat, salt, and volume transports in the eastern Eurasian
677 Basin of the Arctic Ocean, from two years of mooring observations. *ocean-sci-discuss.net*
- 678 Pnyushkov, A. V., I. V. Polyakov, V. V. Ivanov, Y. Aksenov, A. C. Coward, M. Janout, and
679 B. Rabe, 2015: Structure and variability of the boundary current in the Eurasian Basin of
680 the Arctic Ocean. *Deep Sea Research Part I: Oceanographic Research Papers*, **101**, 80–
681 97.
- 682 Polyakov, I. V., and Coauthors, 2011: Fate of early 2000s Arctic warm water pulse. *Bulletin*
683 *of the American Meteorological Society*, **92**, 561–566.
- 684 Price, J. F., R. A. Weller, and R. Pinkel, 1986: Diurnal Cycling - Observations and Models of
685 the Upper Ocean Response to Diurnal Heating, Cooling, and Wind Mixing. *Journal of*
686 *Geophysical Research: Oceans*, **91**, 8411–8427.
- 687 Randelhoff, A., et al., 2015: Seasonal variability and fluxes of nitrate in the surface waters
688 over the Arctic shelf slope. *Geophysical Research*, doi:10.1002/(ISSN)1944-8007.
- 689 Renner, A. H. H., A. Sundfjord, M. A. Janout, R. B. Ingvaldsen, A. B. Möller, R. S. Pickart,
690 R. S. Pickart, and M. D. Pérez-Hernández, 2018: Variability and Redistribution of Heat in
691 the Atlantic Water Boundary Current North of Svalbard. *Journal of Geophysical*
692 *Research: Oceans*, **188**, 11, doi:https://doi.org/10.1029/2018JC013814.
- 693 Rudels, B., 2013: Arctic Ocean circulation, processes and water masses: a description of
694 observations and ideas with focus on the period prior to the International Polar Year
695 2007-2009. *Progress in Oceanography*, **132**, 22–67,
696 doi:http://dx.doi.org/10.1016/j.pocean.2013.11.006.
- 697 Rudels, B., M. Korhonen, U. Schauer, S. Pisarev, B. Rabe, and A. Wisotzki, 2014:
698 Circulation and transformation of Atlantic water in the Eurasian Basin and the
699 contribution of the Fram Strait inflow branch to the Arctic Ocean heat budget. *Progress*
700 *in Oceanography*, **132**, 128–152.
- 701 Schauer, U., and Coauthors, 2002: Confluence and redistribution of Atlantic water in the
702 Nansen, Amundsen and Makarov basins. Vol. 20 of, *Annales Geophysicae*, 257–273.
- 703 Schauer, U., E. Fahrbach, S. Østerhus, and G. Rohardt, 2004: Arctic warming through the

- 704 Fram Strait: Oceanic heat transport from 3 years of measurements. *Journal of*
705 *Geophysical Research: Oceans* (1978--2012), **109**.
- 706 Schauer, U., R. D. Muench, B. Rudels, and L. Timokhov, 1997: Impact of eastern Arctic shelf
707 waters on the Nansen Basin intermediate layers. *Journal of Geophysical Research:*
708 *Oceans* (1978--2012), **102**, 3371–3382.
- 709 Schott, F., and Coauthors, 1996: Observations of Deep Convection in the Gulf of Lions,
710 Northern Mediterranean, during the Winter of 1991/92. [http://dx.doi.org/10.1175/1520-](http://dx.doi.org/10.1175/1520-0485(1996)026<0505:OODCIT>2.0.CO;2)
711 [0485\(1996\)026<0505:OODCIT>2.0.CO;2](http://dx.doi.org/10.1175/1520-0485(1996)026<0505:OODCIT>2.0.CO;2), **26**, 505–524, doi:10.1175/1520-
712 [0485\(1996\)026<0505:OODCIT>2.0.CO;2](http://dx.doi.org/10.1175/1520-0485(1996)026<0505:OODCIT>2.0.CO;2).
- 713 Sundfjord, A., A. H. H. Renner, and A. Beszczynska-Möller, 2017: A-TWAIN mooring
714 hydrography and current data Sep 2012 - Sep 2013 [Data set]. [https://doi.org/10.21334/npolar..deaa](https://doi.org/10.21334/npolar.2017.73d0ea3a),
715 doi:<https://doi.org/10.21334/npolar.2017.73d0ea3a>.
- 716 Våge, K., R. S. Pickart, V. Pavlov, P. Lin, D. J. Torres, R. Ingvaldsen, A. Sundfjord, and A.
717 Proshutinsky, 2016: The Atlantic Water boundary current in the Nansen Basin: Transport
718 and mechanisms of lateral exchange. *Journal of Geophysical Research: Oceans*, **121**,
719 6946–6960, doi:10.1002/2016JC011715.
- 720 Zhao, M., M. L. Timmermans, S. Cole, R. Krishfield, A. Proshutinsky, and J. Toole, 2014:
721 Characterizing the eddy field in the Arctic Ocean halocline. *Journal of Geophysical*
722 *Research: Oceans*, **119**, 8800–8817, doi:10.1002/2014JC010488.

723

724

725

726

727

728

729 **TABLES**

730 Table 1: Instruments contained on each mooring together with their sampling details. The
 731 third column shows the depth of the instrument; for the MicroCats the depth shown is the
 732 average depth measured. Time is Coordinated Universal Time (UTC). The “NPI1” and
 733 “NPI2” are called “A200” and “A800” in Renner et al. (2018).

734

	Instrument	Depth (m)	Starting time	Interval	Ending time
NPI1	SBE37 MicroCat	52	Flooded		
	SBE37 MicroCat	104	16-Sep-2012 17:45	15 minutes.	15-Sep-2013 17:00
	Workhorse 150kHz ADCP	112	16-Sep-2012 06:45	20 minutes	15-Sep-2013 10:05
	SBE37 MicroCat	131	16-Sep-2012 17:45	15 minutes	15-Sep-2013 17:00
	SBE37 MicroCat	180	16-Sep-2012 17:45	15 minutes	15-Sep-2013 17:00
NPI2	SBE16 SeaCat	25	18-Sep-2012 22:00	15 minutes.	16-Sep-2013 10:15
	SBE16 SeaCat	49	18-Sep-2012 22:00	15 minutes	06-Sep-2013 23:45
	Workhorse 300kHz ADCP	84	18-Sep-2012 06:09	20 minutes	03-Sep-2013 10:09
	SBE37 MicroCat	101	18-Sep-2012 12:30	15 minutes	16-Sep-2013 12:30
	SBE37 MicroCat	198	18-Sep-2012 12:30	15 minutes	16-Sep-2013 10:15
	ADCP 190kHz	244	20-Sep-2012 10:10	20 minutes	16-Sep-2013 13:50
	ADCP 190kHz	390	Failed		
	SBE37 MicroCat	399	18-Sep-2012 12:30	15 minutes	16-Sep-2013 10:15
	RCM7	402	18-Sep-2012 14:00	1 hour	16-Sep-2013 09:00
	SBE37 MicroCat	751	18-Sep-2012 12:30	15 minutes	16-Sep-2013 10:15
	RCM7	754	18-Sep-2012 14:00	1 hour	16-Sep-2013 09:00
WHOI1	Workhorse 300kHz ADCP	50	13-Sep-2012 12:00	1 hour	30-Aug-2013 22:00
	Long Ranger 75kHz ADCP	53	13-Sep-2012 12:00	1 hour	17-Sep-2013 09:00
	MMP	60-1280	24-Sep-2012 00:28	12 hour	16-Sep-2013 12:41
WHOI2	Workhorse 300kHz ADCP	50	19-Sep-2012 12:00	1 hour	15-Sep-2013 09:00
	Long Ranger 75kHz ADCP	53	13-Sep-2012 12:00	1 hour	17-Sep-2013 17:00
	MMP	60-1280	24-Sep-2012 00:33	12 hours	17-Sep-2013 00:49
WHOI3	Workhorse 300kHz ADCP	50	14-Sep-2012 05:00	1 hour	1-Sep-2013 10:00
	Long Ranger 75kHz ADCP	53	13-Sep-2012 12:00	1 hour	9-Aug-2013 00:00
	MMP	60-1280	24-Sep-2012 00:00	12 hours	18-Sep-2013 12:12
WHOI4	Workhorse 300kHz ADCP	50	13-Sep-2012 12:00	1 hour	19-Sep-2013 18:00
	Long Ranger 75kHz ADCP	53	13-Sep-2012 12:00	1 hour	12-Sep-2013 06:00
	MMP	60-1280	24-Sep-2012 00:39	12 hours	19-Sep-2013 00:02

735

736

737 Table 2: Instruments accuracy

	Conductivity	Temperature	Velocity
SBE37 MicroCat	± 0.0003 S/m	± 0.002 °C (-5 to to 35 °C);	
SBE16 SeaCat	± 0.001 S/m	± 0.01 °C	
ADCP 150kHz			1% of measured value
ADCP 190kHz			1% of measured value
Long Ranger 75kHz ADCP			$\pm 1\% \pm 5$ mm/s
Workhorse 300kHz ADCP			0.5% of the water velocity relative to ADCP ± 0.5 cm/s 0.1cm/s ± 5 m/s (default) ± 20 m/s (max) 1–255
MMP (SBE37 MicroCat)	± 0.0003 S/m	± 0.002 °C (-5 to to 35 °C);	
RCM7	$\pm 0.1\%$ of range.	± 0.05 °C	± 1 cm/s or $\pm 4\%$ of actual speed whichever is greater.

738

739

740

741
742

743 Table 3: Average eastward volume transports for the different water masses: year round
744 average (second column) and for the different ice seasons (last two columns).

745

Water Mass	Average	Open water	Full ice cover
AW	2.08 ± 0.24	2.44 ± 0.12	1.10 ± 0.06
PSW _w	0.26 ± 0.12	0.32 ± 0.00	0.27 ± 0.00
AIW	0.99 ± 0.18	0.46 ± 0.07	0.88 ± 0.05
Total	3.96 ± 0.32	3.30 ± 0.13	2.32 ± 0.06

746
747

748

749 **List of Figures**

- 750 1. (a) Geographical map of the region where Atlantic Water enters the Arctic Ocean. The
751 schematic circulation of the Atlantic Water is indicated by the red lines. Part of the West
752 Spitsbergen Current (WSC) recirculates in Fram Strait, and three branches ultimately
753 emerge from the strait: one flows around the Yermak Plateau (YB), one flows through
754 Yermak Pass (YPB), and one flows north of Svalbard (SB). The yellow box indicates
755 the A-TWAIN study area; the mooring array is denoted by the green line (see Figure 2
756 for the individual mooring sites). The yellow dot and star show the position of the
757 additional upstream moorings used in the study: the Fram Strait and IOPAN mooring.
758 The IBCAO version 3 bathymetry is shaded according to the colorbar. (b) Vertical
759 section showing the instrumentation of the array (see the legend). The names of the
760 moorings are indicated along the top.
- 761 2. Vertically averaged velocities at the mooring sites together with their standard ellipses
762 for three time periods: a) Year-long average; b) Open water period; and c) Full ice cover
763 period. The average sea ice concentration for each time period is shown by the white
764 contours. The IBCAO version 3 bathymetry is shaded according to the colorbar.
- 765 3. (a) Year-long averaged wind speed (left axis) and percent sea ice coverage (right axis).
766 (b-d) Year-long averaged vertical sections of potential temperature, salinity, and
767 absolute geostrophic velocity (color). The average potential density is shown by the
768 black contours. The grey contours in (d) correspond to 1 cm/s increments in velocity.
769 The dashed lines denote the boundaries of the AW layer. The triangles along the top of
770 the sections labeled N and W indicate the NPI and WHOI moorings, respectively. The
771 10% value of the core velocity lies near the 2 cm/s isoline.
- 772 4. (a,b) The two extreme states of the boundary current associated with EOF mode 1,
773 determined by adding the maximum/minimum values of the mode into the mean vertical

774 section of absolute geostrophic velocity. The triangles along the top of the sections
775 labeled N and W indicate the NPI and WHOI moorings, respectively. (c) The temporal
776 amplitude of the mode.

777 5. (a) Wind rose, and (b) time series of wind vectors, calculated using the Era-Interim
778 reanalysis data. (c) MASAM2 Sea Ice concentration across the mooring array. The
779 green lines mark the different ice regimes discussed in the text. (d) Average temperature
780 (blue curve), salinity (red curve), and volume transport (black curve) of the AW layer
781 in the boundary current.

782 6. Composite vertical sections of potential temperature (top row), salinity (second row),
783 Brunt-Väisälä frequency (third row) and absolute geostrophic velocity (bottom row) for
784 the open water (left column) and full ice cover (right column) periods discussed in the
785 text. The white dashed lines denote the boundaries of the AW layer. The triangles along
786 the top of the sections labeled N and W indicate the NPI and WHOI moorings,
787 respectively.

788 7. Time series of (a) potential temperature and (b) salinity for the AW layer measured at
789 the A-TWAIN study site (blue) and the IOPAN mooring (gray). The AW temperature
790 at 117 m in Fram Strait is shown in black. The Fram Strait time series has been lagged
791 by two months relative to the other two time series.

792 8. (a) Representative density profiles in January 2013 from the WHOI-1 mooring (green)
793 and the IOPAN mooring (black), where the depth of the mixed-layer is indicated by the
794 dot. (b) Time series of mixed-layer depth at the WHOI-1 mooring (green dots) and the
795 IOPAN mooring (black dots).

796 9. Simulated mixed-layer depth from the PWP model forced with the ERA-Interim heat
797 flux time series (red line) for the A-TWAIN WHOI1 mooring, together with the

798 observed mixed-layer depth at the WHOI1 site (black line and dots). Times with no
799 MLD are indicated by the grey lines at the top of the plot.

800 10. (a) Time series of percent sea ice coverage averaged over the A-TWAIN array. (b)
801 Time-depth plot of potential temperature anomaly relative to the first profile. (c) Same
802 as (b) except for salinity. The green dots indicate the mixed-layer depths, and the black
803 dots denote the boundaries of the AW layer. See the text for details. The signal at 360
804 m is due to the initial average profile, as it has a local minimum in temperature and
805 salinity at that depth

806 11. Time series of mixed-layer depth for the periods when the sea ice concentration is (a)
807 greater than 85%, (b) less than 10%, and (c) between 10-85%, for the A-TWAIN array
808 (green dots) and the upstream IOPAN mooring (black dots).

809 12. (a) Evolution of the average T/S of the mixed-layer over the course of the year for the
810 IOPAN mooring (see the legend). The circles denote the average value for each month
811 (there is no mixed layer present during the month of July). The different water masses
812 are: PSW = polar surface water; iPSW = inshore polar surface water; PSWw = warm
813 polar surface water; AW = Atlantic water; and AIW = Arctic intermediate water. (b)
814 Same as (a) except for the portion of the AW layer beneath the mixed-layer. Potential
815 density contours are dashed.

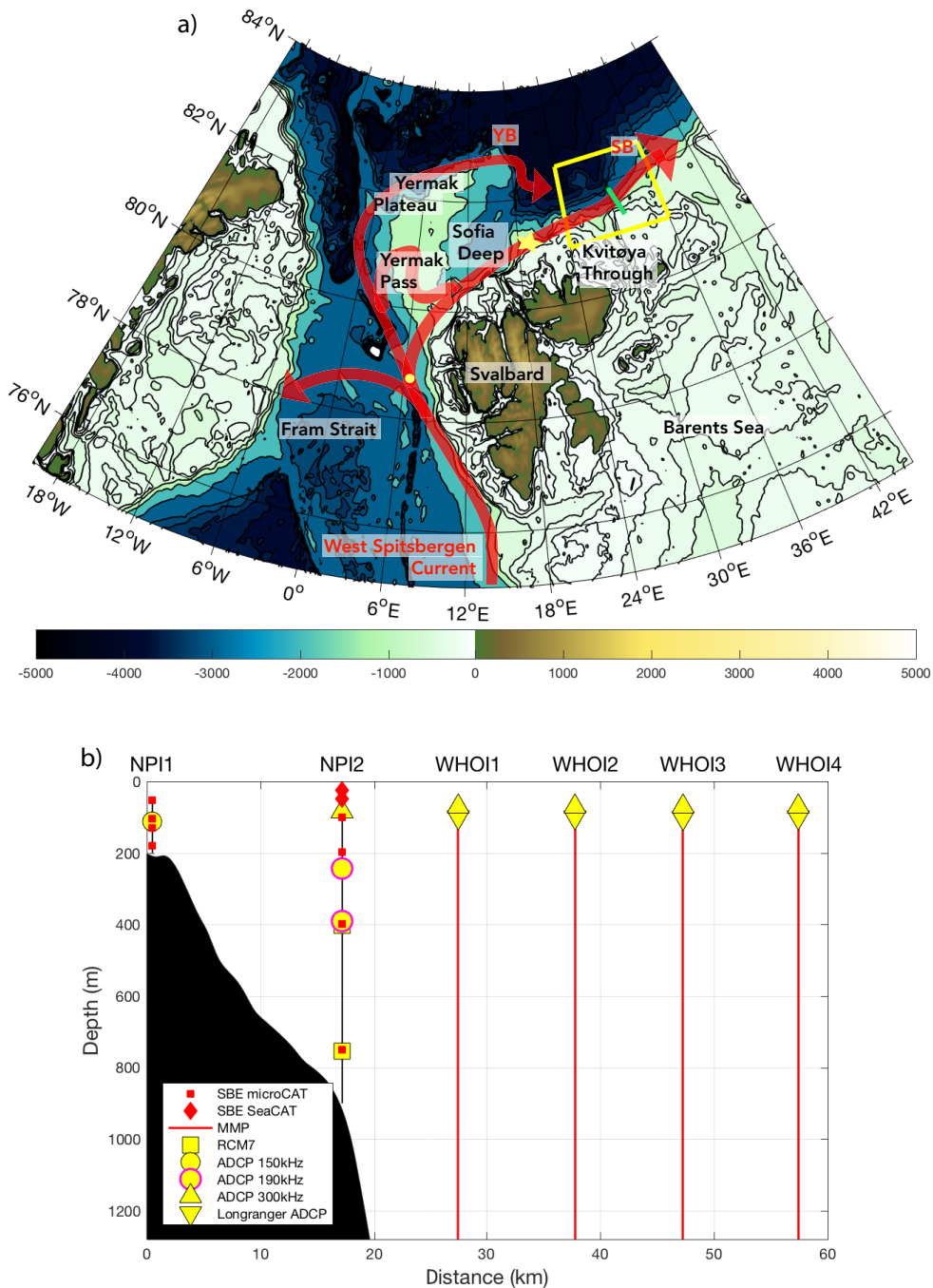


Figure 1: (a) Geographical map of the region where Atlantic Water enters the Arctic Ocean. The schematic circulation of the Atlantic Water is indicated by the red lines. Part of the West Spitsbergen Current (WSC) recirculates in Fram Strait, and three branches ultimately emerge from the strait: one flows around the Yermak Plateau (YB), one flows through Yermak Pass (YPB), and one flows north of Svalbard (SB). The yellow box indicates the A-TWAIN study area; the mooring array is denoted by the green line (see Figure 2 for the individual mooring sites). The yellow dot and star show the position of the additional upstream moorings used in the study: the Fram Strait and IOPAN mooring. The IBCAO version 3 bathymetry is shaded according to the colorbar. (b) Vertical section showing the instrumentation of the array (see the legend). The names of the moorings are indicated along the top.

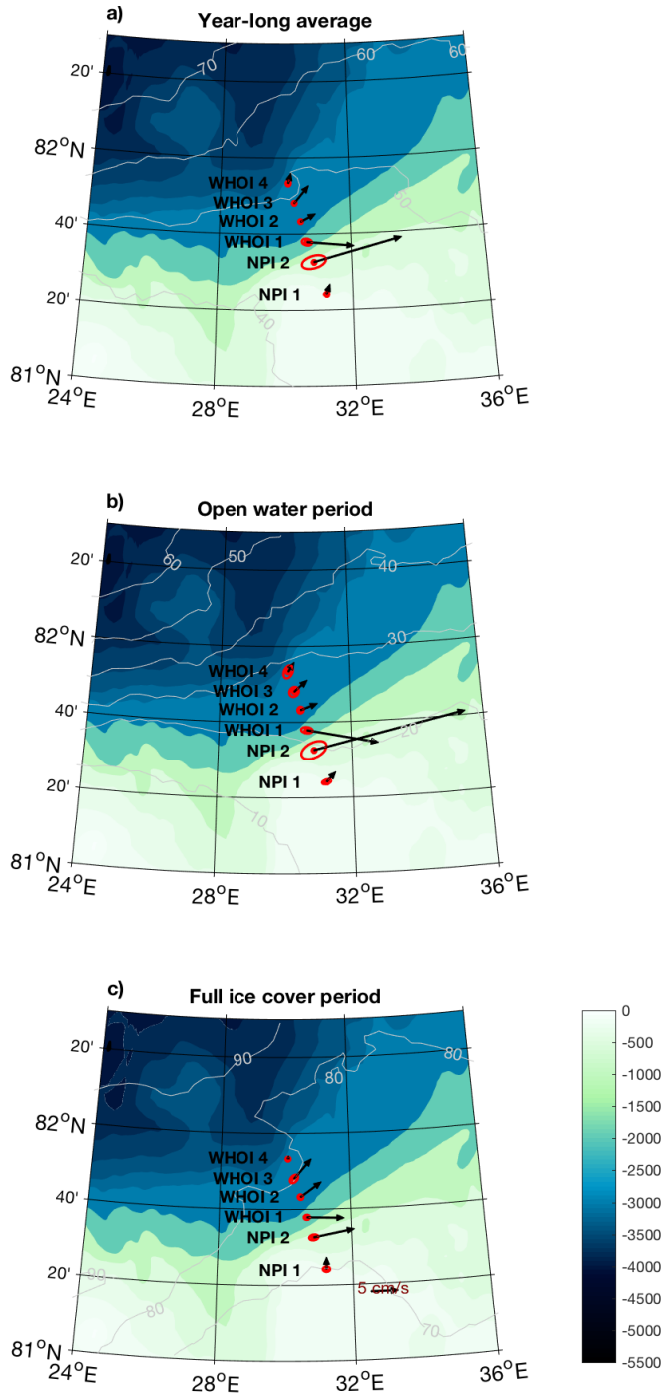


Figure 2: Vertically averaged velocities at the mooring sites together with their standard ellipses for three time periods: a) Year-long average; b) Open water period; and c) Full ice cover period. The average sea ice concentration for each time period is shown by the white contours. The IBCAO version 3 bathymetry is shaded according to the colorbar.

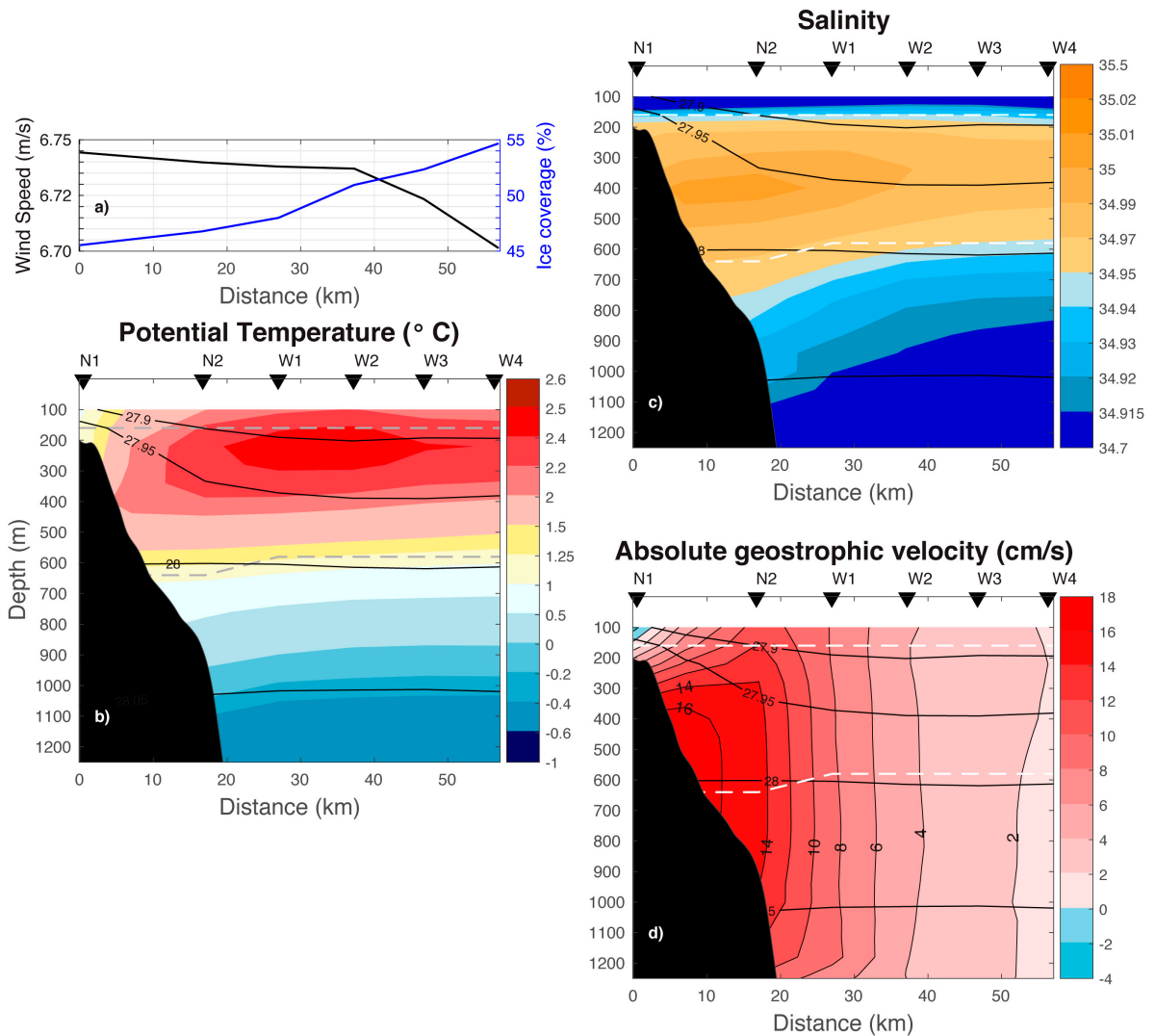


Figure 3: (a) Year-long averaged wind speed (left axis) and percent sea ice coverage (right axis). (b-d) Year-long averaged vertical sections of potential temperature, salinity, and absolute geostrophic velocity (color). The average potential density is shown by the black contours. The grey contours in (d) correspond to 1 cm/s increments in velocity. The dashed lines denote the boundaries of the AW layer. The triangles along the top of the sections labeled N and W indicate the NPI and WHOI moorings, respectively. The 10% value of the core absolute velocity corresponds to the 2 cm/s isoline.

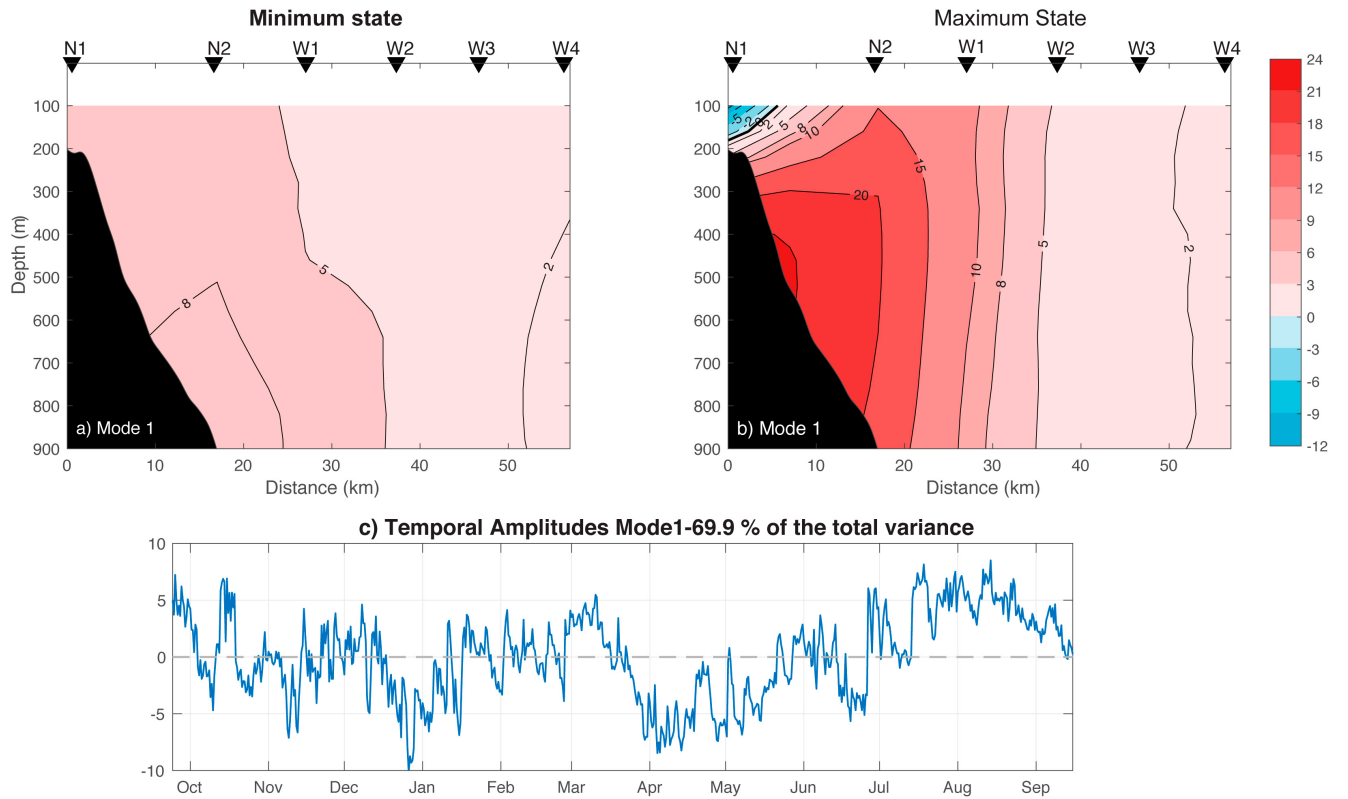


Figure 4: (a,b) The two extreme states of the boundary current associated with EOF mode 1, determined by adding the maximum/minimum values of the mode into the mean vertical section of absolute geostrophic velocity. The triangles along the top of the sections labeled N and W indicate the NPI and WHOI moorings, respectively. (c) The temporal amplitude of the mode.

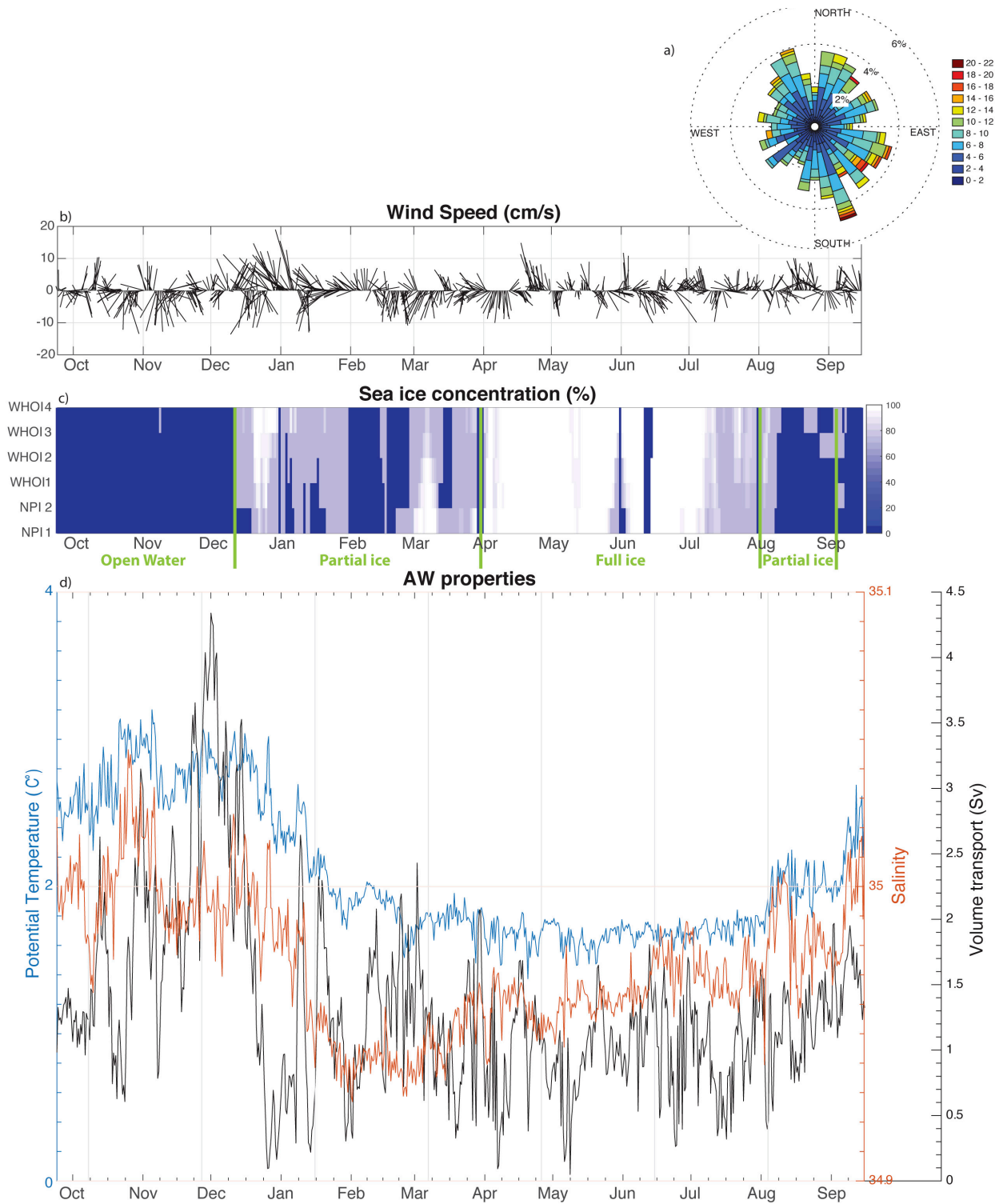


Figure 5: (a) Wind rose, and (b) timeseries of wind vectors, calculated using the Era-Interim reanalysis data. (c) MASAM2 Sea Ice concentration across the mooring array. The green lines mark the different ice regimes discussed in the text. (d) Average temperature (blue curve), salinity (red curve), and volume transport (black curve) of the AW layer in the boundary current.

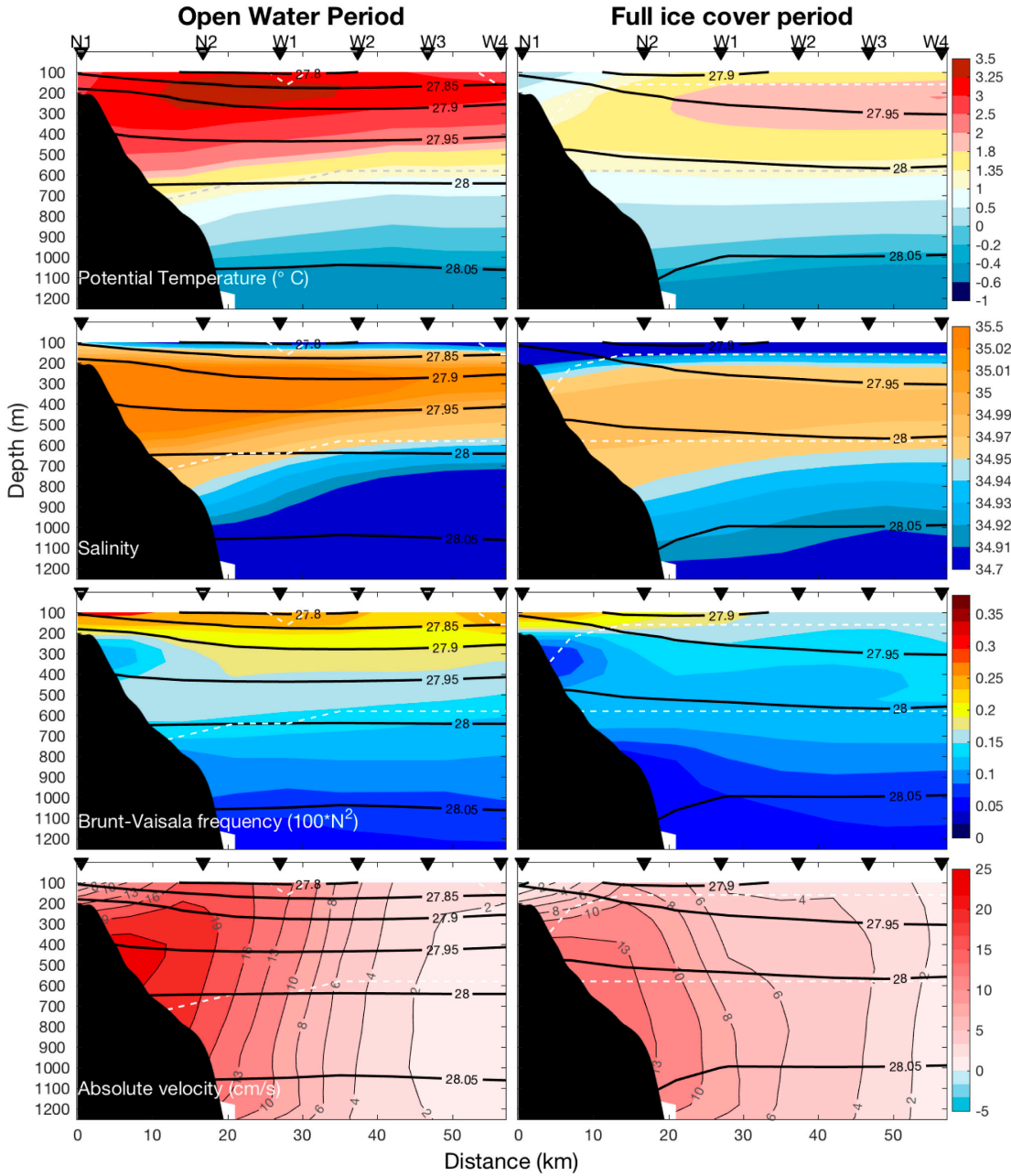


Figure 6: Composite vertical sections of potential temperature (top row), salinity (second row), Brunt-Väisälä frequency (third row) and absolute geostrophic velocity (bottom row) for the open water (left column) and full ice cover (right column) periods discussed in the text. The white dashed lines denote the boundaries of the AW layer. The triangles along the top of the sections labeled N and W indicate the NPI and WHOI moorings, respectively.

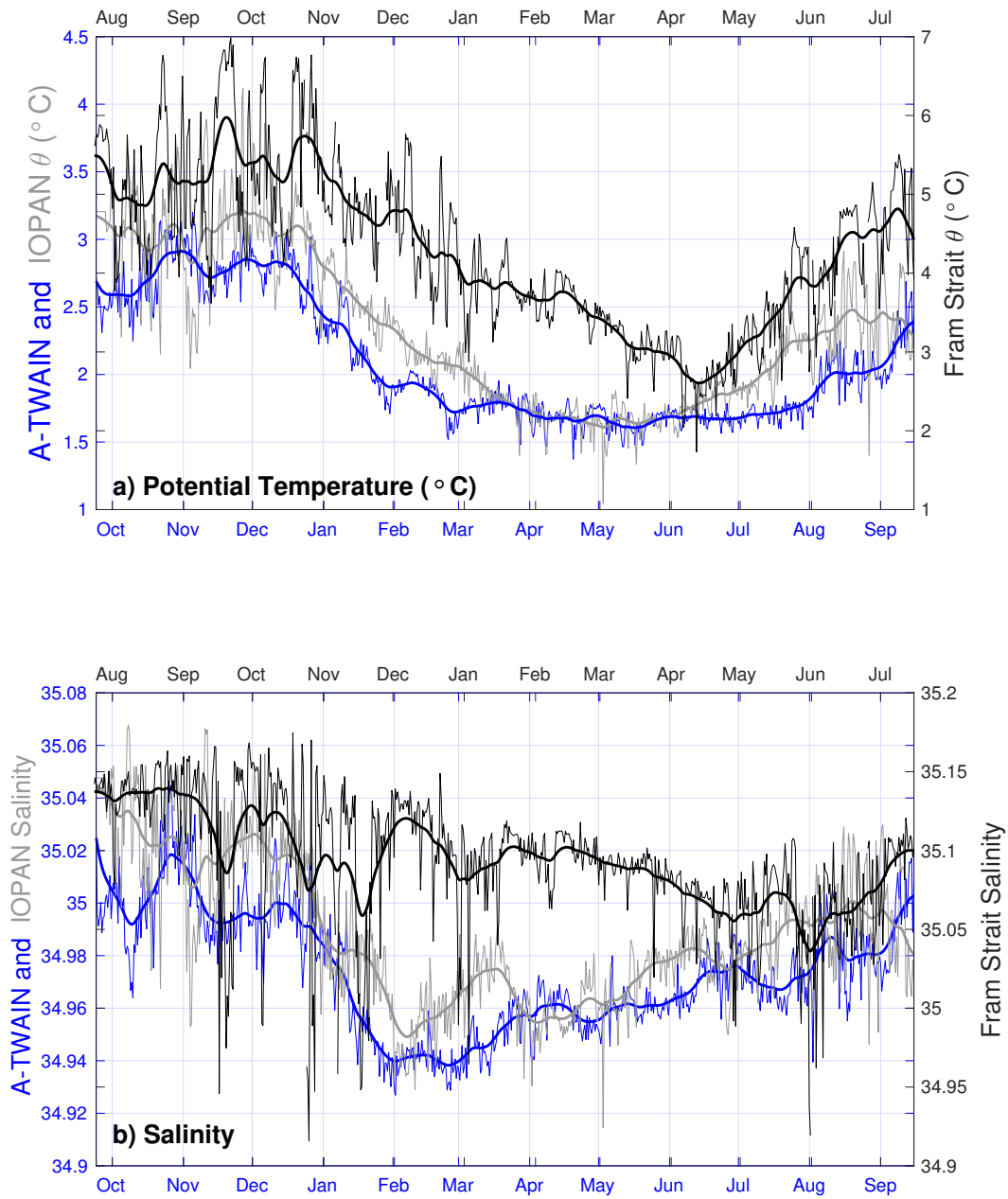


Figure 7: Time series of (a) potential temperature and (b) salinity for the AW layer measured at the A-TWAIN study site (blue) and the IOPAN mooring (gray). The AW temperature at 117 m in Fram Strait is shown in black. The Fram Strait time series has been lagged by two months relative to the other two time series.

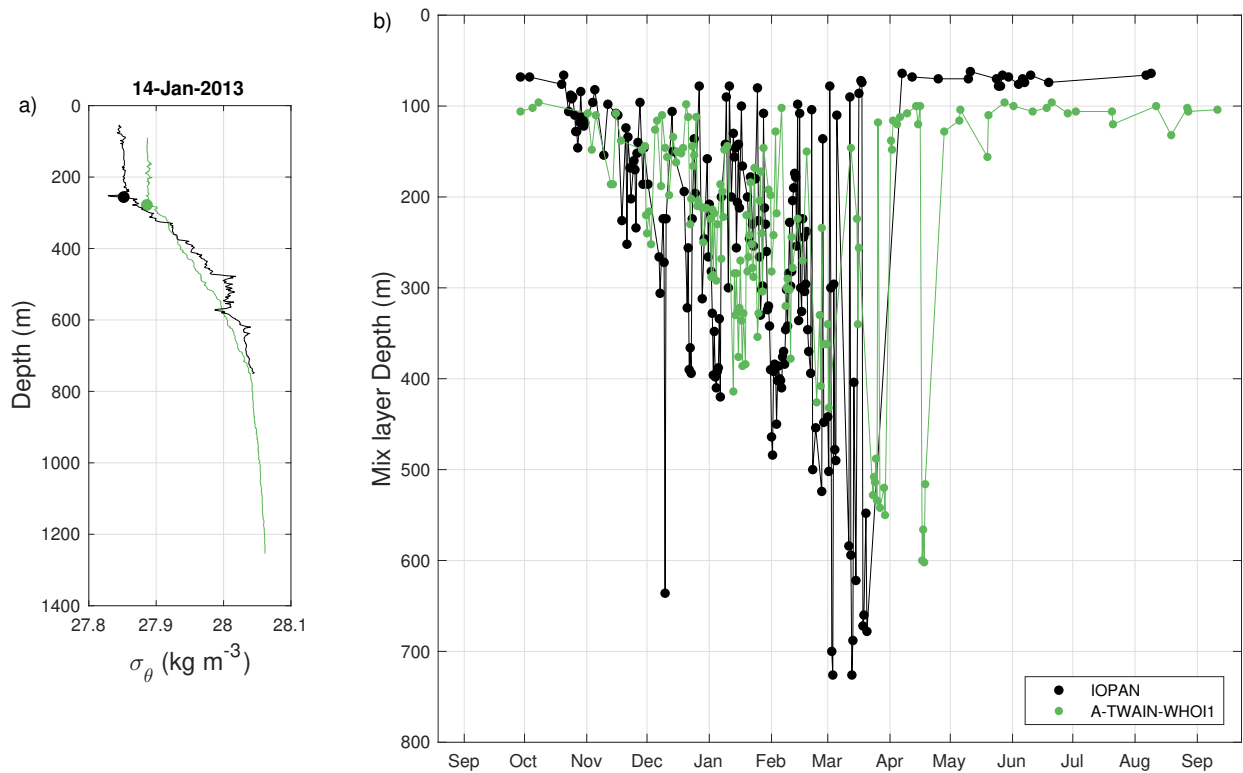


Figure 8: (a) Representative density profiles in January 2013 from the WHOI-1 mooring (green) and the IOPAN mooring (black), where the depth of the mixed-layer is indicated by the dot. (b) Time series of mixed-layer depth at the WHOI-1 mooring (green dots) and the IOPAN mooring (black dots).

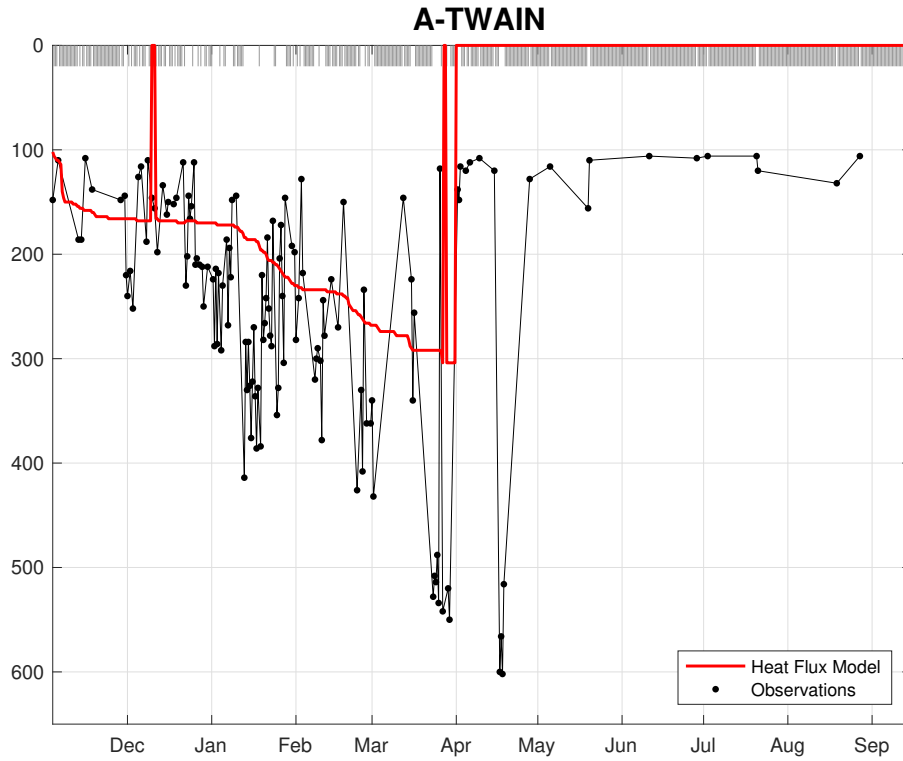


Figure 9: Simulated mixed-layer depth from the PWP model forced with the ERA-Interim heat flux time series (red line) for the A-TWAIN WHOI1 mooring, together with the observed mixed-layer depth at the WHOI1 site (black line and dots). Times with no MLD are indicated by the grey lines at the top of the plot.

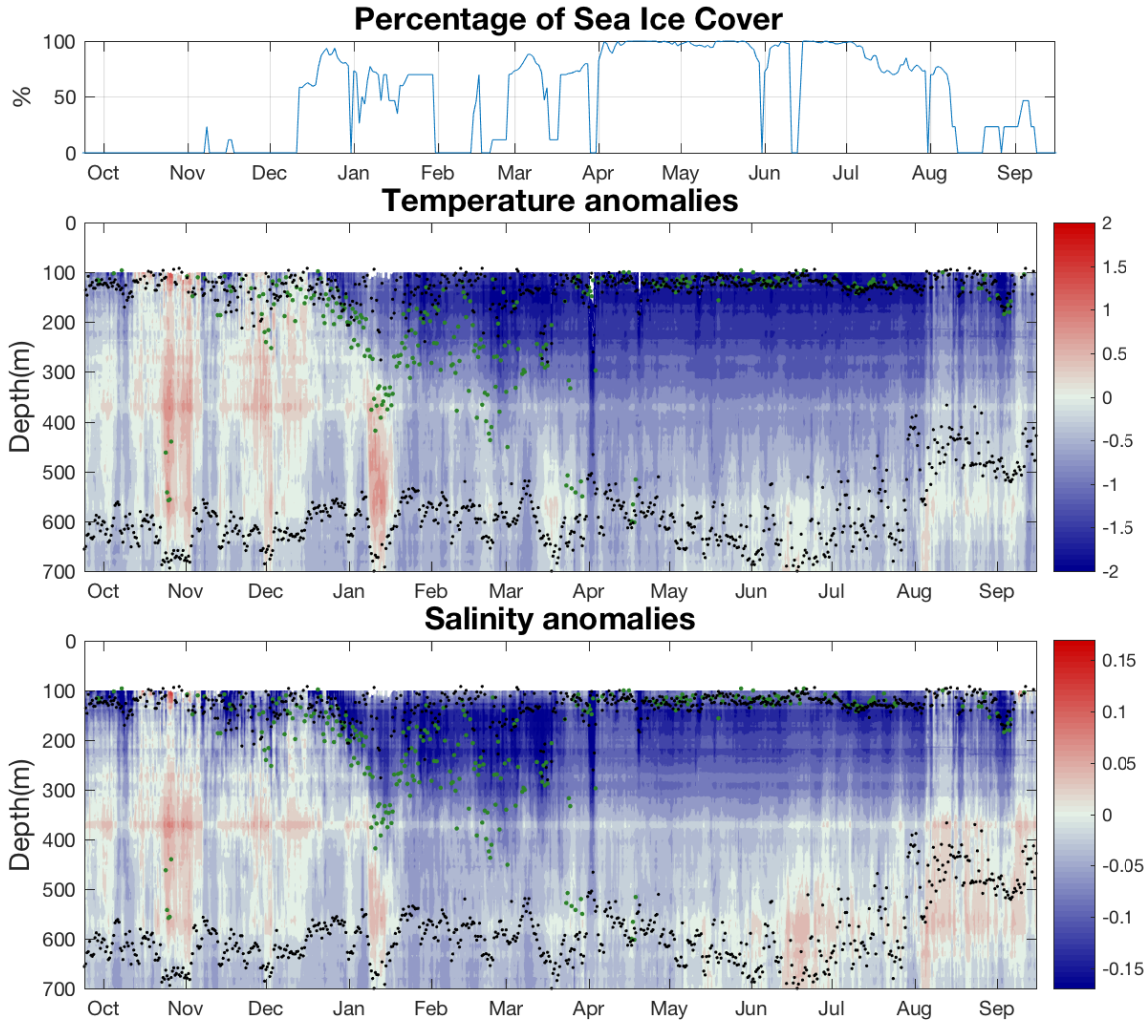


Figure 10: (a) Time series of percent sea ice coverage averaged over the A-TWAIN array. (b) Time-depth plot of potential temperature anomaly relative to the first profile. (c) Same as (b) except for salinity. The green dots indicate the mixed-layer depths, and the black dots denote the boundaries of the AW layer. See the text for details. The signal at 360 m is due to the initial average profile, as it has a local minimum in temperature and salinity at that depth.

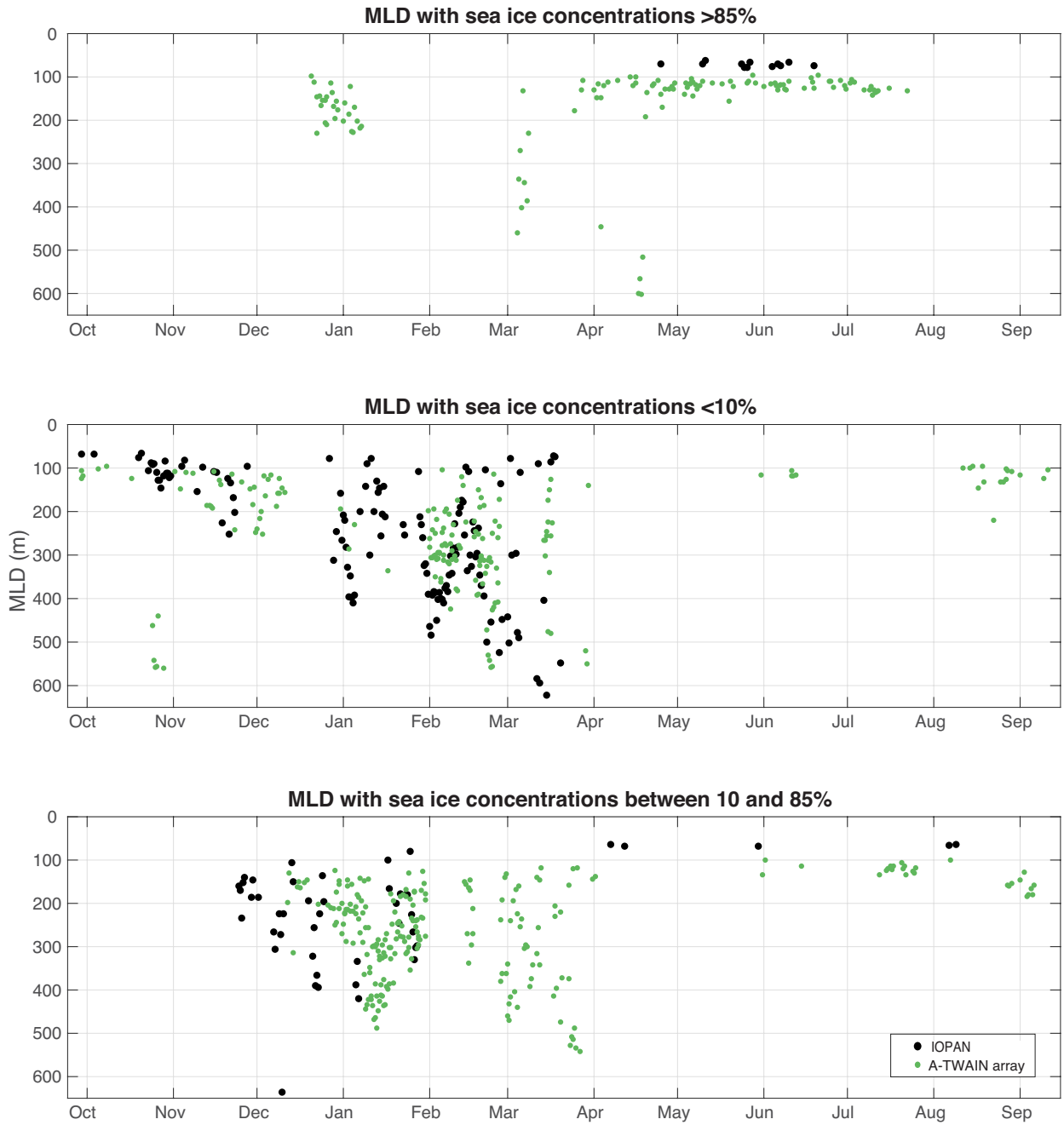


Figure 11: Time series of mixed-layer depth for the periods when the sea ice concentration is (a) greater than 85%, (b) less than 10%, and (c) between 10-85%, for the A-TWAIN array (green dots) and the upstream IOPAN mooring (black dots).

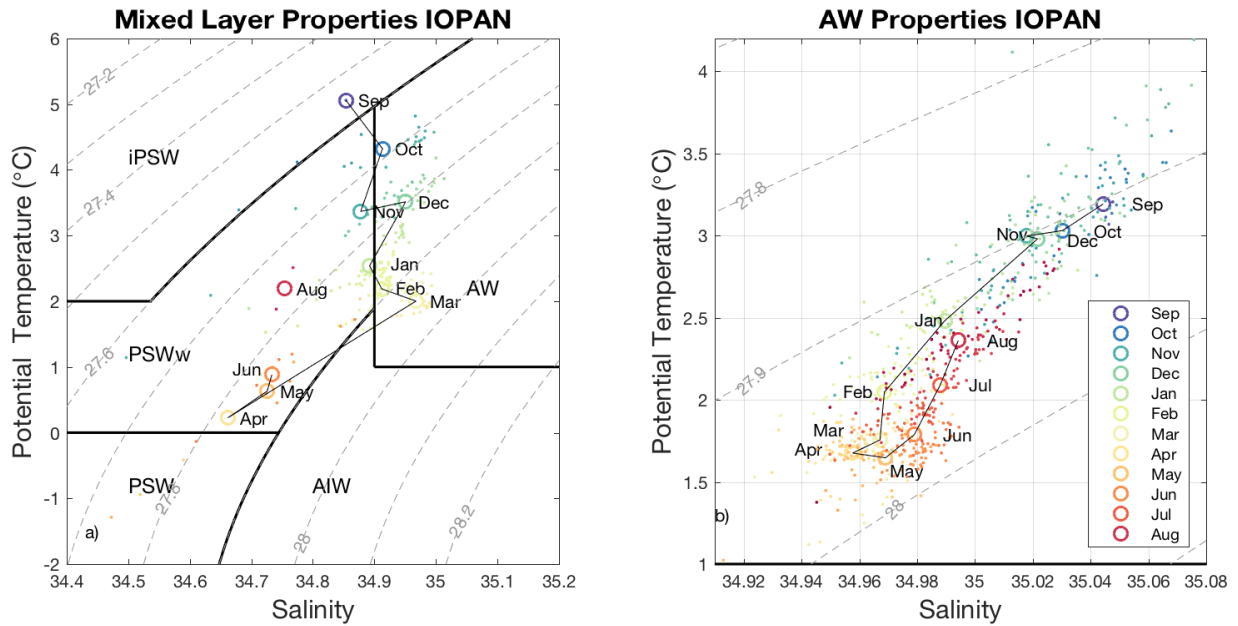


Figure 12: (a) Evolution of the average T/S of the mixed-layer over the course of the year for the IOPAN mooring (see the legend). The circles denote the average value for each month (there is no mixed layer present during the month of July). The different water masses are: PSW = polar surface water; iPSW = inshore polar surface water; PSWw = warm polar surface water; AW = Atlantic water; and AIW = Arctic intermediate water. (b) Same as (a) except for the portion of the AW layer beneath the mixed-layer. Potential density contours are dashed.